ION CHANNELS

Local Ca^{2+} signals couple activation of TRPV1 and ANO1 sensory ion channels

Shihab Shah[1], Chase M. Carver[2], Pierce Mullen[1], Stephen Milne[1], Viktor Lukacs[1], Mark S. Shapiro[2], Nikita Gamper[1,3]*

Copyright © 2020 The Authors, some rights reserved; exclusive licensee American Association for the Advancement of Science. No claim to original U.S. Government Works

ANO1 (TMEM16A) is a Ca^{2+}-activated Cl^- channel (CaCC) expressed in peripheral somatosensory neurons that are activated by painful (noxious) stimuli. These neurons also express the Ca^{2+}-permeable channel and noxious heat sensor TRPV1, which can activate ANO1. Here, we revealed an intricate mechanism of TRPV1-ANO1 channel coupling in rat dorsal root ganglion (DRG) neurons. Simultaneous optical monitoring of CaCC activity and Ca^{2+} dynamics revealed that the TRPV1 ligand capsaicin activated CaCCs. However, depletion of endoplasmic reticulum (ER) Ca^{2+} stores reduced capsaicin-induced Ca^{2+} increases and CaCC activation, suggesting that ER Ca^{2+} release contributed to TRPV1-induced CaCC activation. ER store depletion by plasma membrane–localized TRPV1 channels was demonstrated with an ER-localized Ca^{2+} sensor in neurons exposed to a cell-impermeable TRPV1 ligand. Proximity ligation assays established that ANO1, TRPV1, and the IP_3 receptor IP_3R1 were often found in close proximity to each other. Stochastic optical reconstruction microscopy (STORM) confirmed the close association between all three channels in DRG neurons. Together, our data reveal the existence of ANO1-containing multichannel nanodomains in DRG neurons and suggest that coupling between TRPV1 and ANO1 requires ER Ca^{2+} release, which may be necessary to enhance ANO1 activation.

INTRODUCTION

Ca^{2+}-activated Cl^- channels (CaCCs) are important regulators of epithelial transport, smooth muscle contraction, and neuronal excitability [reviewed in (*1*–*4*)]. The molecular identity of CaCCs remained elusive until 2008, when three groups identified ANO1 (TMEM16A), a member of the anoctamin (TMEM16) family of transmembrane proteins, as a bona fide CaCC (*5*–*7*). Functional expression of ANO1 has been confirmed in peripheral damage-sensing (nociceptive) neurons (*7*–*10*). In contrast to most adult CNS neurons, peripheral somatosensory neurons accumulate relatively high intracellular $[Cl^-]_i$, sufficient to maintain their Cl^- equilibrium potential (E_{Cl}) at voltages more positive than the threshold for action potential firing (*8*, *11*). Therefore, activation of ANO1-mediated CaCCs in these cells can increase excitability and trigger or potentiate nociception. Furthermore, the Na^+, K^+, and Cl^- cotransporter NKCC1 is up-regulated in sensory neurons during nerve injury (*12*), which leads to further Cl^- accumulation and potentially even greater excitatory effects of ANO1 currents.

ANO1 channels have an intrinsically low Ca^{2+} sensitivity with a half-maximal effective concentration (EC_{50}) in the range of 2 to 5 μM at −60 mV (*7*, *13*). This low sensitivity may be due to the unusual location of the Ca^{2+} binding site of ANO1, which localizes to a domain between the α6 and α8 transmembrane helices situated within the lipid bilayer (*14*). The Ca^{2+} sensitivity of ANO1 is voltage dependent such that it increases with depolarization (*13*, *15*); for example, an EC_{50} of 0.4 μM is measured at +100 mV. Nevertheless, at the resting membrane potential of sensory neurons of ~−60 mV (*16*–*18*), $[Ca^{2+}]_i$ of >1 to 2 μM is required to activate ANO1. Global Ca^{2+} levels in the cytosol do not normally reach micromolar concentrations, and therefore, to enable reliable ANO1 activation, localized, high-intensity Ca^{2+} signals are required (*1*, *19*–*21*). In sensory neurons from dorsal root ganglion (DRG), ANO1 is found in close proximity to G protein–coupled receptors (GPCRs), such as the bradykinin (BK) B_2 receptor (B_2R) and the protease-activated receptor-2 (PAR2) on the plasma membrane (PM), and physically coupled with endoplasmic reticulum (ER)–localized IP_3 receptors (IP_3Rs), forming a junctional ER-PM complex (*19*). We have shown that upon stimulation of such $G_{q/11}$-coupled GPCRs (G_qPCRs), IP_3 generation activates IP_3Rs, which, in turn, leads to Ca^{2+} release from the ER and ANO1 activation. Because of the proximity between the components of the junctional complex, local Ca^{2+} elevations, which reach up to 50 to 75 μM at the mouth of IP_3R channel (*22*, *23*), are sufficient to enable ANO1 activation (*19*). BK, proteases, and other relevant GPCR ligands are released upon tissue inflammation and contribute to inflammatory pain and itch, in part through the GPCR-induced activation of ANO1/CaCCs and depolarization of nociceptive afferents (*8*, *24*–*27*). Localization of ANO1 channels to ER-PM junctional nanodomains may also serve the function of shielding ANO1 channels from activation by other, non-colocalized Ca^{2+} signals, such as those generated by voltage-gated Ca^{2+} channels (VGCCs) during action potential firing (*1*, *19*, *28*).

ANO1 in DRG neurons can also be activated by noxious heat at a similar temperature range to the "canonical" noxious heat sensor, transient receptor potential cation channel subfamily V member 1 (TRPV1) (*9*, *10*). In addition, TRPV1 is another major mediator of inflammatory pain, and activation of TRPV1 channels is sensitized by BK and PAR2 (*25*, *29*). Furthermore, opening of TRPV1 channels activates ANO1 in sensory neurons (*10*). The latter study suggested that ANO1 and TRPV1 are directly coupled, with Ca^{2+} entry through TRPV1 providing the local Ca^{2+} elevation that allows ANO1 activation (*10*). However, the Ca^{2+} influx through TRPV1 amounts to no more than ~10% of the total TRPV1 cation current (*30*). On the other hand, TRPV1 activates Ca^{2+}-sensitive phospholipase C (PLCδ) and induces Ca^{2+} release from the ER in the absence of prior stimulation

[1]School of Biomedical Science, Faculty of Biological Sciences, University of Leeds, Leeds, LS2 9JT, UK. [2]Department of Cell and Integrative Physiology, University of Texas Health San Antonio, San Antonio, TX 78229, USA. [3]Department of Pharmacology, Hebei Medical University, Shijiazhuang 050017, People's Republic of China. *Corresponding author. Email: n.gamper@leeds.ac.uk

Downloaded from http://stke.sciencemag.org/ on May 3, 2020

of G_qPCRs (*31*). Thus, the question arises: Is direct Ca^{2+} influx through the TRPV1 channel pore sufficient to fully activate ANO1 in sensory neurons or are other Ca^{2+} sources also involved or obligatory? Using live-imaging approaches, patch-clamp electrophysiology, proximity ligation, and a superresolution microscopy method, we demonstrated that a substantial fraction of ANO1 and TRPV1 channels were found in junctional nanodomains in small-diameter nociceptors and that TRPV1-mediated Ca^{2+} release from ER-resident IP_3Rs was a major factor in functional TRPV1-ANO1 coupling.

RESULTS

Single-cell fluorescence imaging can measure currents through CaCCs

Imaging of halide-sensitive enhanced yellow fluorescent protein (EYFP) mutants has been previously used to monitor Cl^- channel activity (*32*–*34*). The method is based on the permeability of most anion channels to iodide ions (I^-), which, when added to the extracellular solution, quench EYFP fluorescence in a manner dependent on anion channel opening. However, previous applications of this technique, including a single-cell approach developed by us (*19*), do not allow correlation of intracellular Ca^{2+} dynamics with I^- influx. Furthermore, the agonist-independent quenching complicates quantification and masks the responses produced by agonists. Here, we developed a triple-wavelength imaging approach to simultaneously monitor halide-sensitive EYFP quenching and ratiometric fura-2 Ca^{2+} imaging (Fig. 1A). DRG neurons abundantly express γ-aminobutyric acid type A ($GABA_A$) Cl^- channels (*35*–*37*); thus, we used GABA responses from cultured rat DRG neurons transfected with the halide-sensitive mutant EYFP H148Q/I152L (EYFP-QL) to optimize the extracellular I^- concentration and minimize agonist-independent quenching (Fig. 1, B to E). Equimolar replacement of 5 to 30 mM NaCl with NaI revealed that 5 mM NaI offered the lowest rate of agonist-independent EYFP-QL quenching while providing sufficient dynamic range for the reliable detection of Cl^- channel opening.

We then performed simultaneous halide and Ca^{2+} imaging of DRG neurons transfected with EYFP-QL and loaded with fura-2-acetoxymethyl ester (fura-2 AM). B_2R receptors were stimulated by bath application of BK (250 nM) in the presence of 5 mM NaI while performing triple-wavelength excitation (340/380/488 nm). Consistent with our previous study (*19*), BK induced robust transient $[Ca^{2+}]_i$ rises, which were temporally correlated with the EYFP-QL fluorescence quenching (Fig. 2, A and B). In contrast to the Ca^{2+} rises, which were transient in nature, the EYFP-QL quenching did not normally recover within the period of observation (reflecting that once I^- is taken up by a cell during CaCC activation, it is not easily extruded under our experimental conditions). The mean amplitude of the peak fura-2 Ca^{2+} signal ($\Delta R/R_0$) and the mean drop in the normalized EYFP-QL fluorescence ($\Delta F/F_0$) induced by BK are shown in Fig. 2C (left).

To confirm that this quenching was mediated by ANO1 and not another Cl^- channel flux, transfected cells were preincubated and perfused with two ANO1 inhibitors, T16A-inhA01 and Ani9 (*38*). In the presence of T16A-inhA01 (50 μM), EYFP-QL quenching induced by BK was abolished despite the presence of Ca^{2+} transients (Fig. 2C). Ani9 (500 nM) also inhibited BK-induced quenching, although to a lesser extent. The BK-induced $[Ca^{2+}]_i$ rises were smaller in the presence of both ANO1 inhibitors, compared to control conditions (Fig. 2C). This observation is consistent with the hypothesis that ANO1 is not only a target of the Ca^{2+} signals but may also facilitate ER Ca^{2+} release because of structural interactions between the PM and the ER (*28*). Hence, both T16A-inhA01 and Ani9 may interfere with this process. However, BK application still induced measurable rises in $[Ca^{2+}]_i$ in the presence of T16A-inhA01 and Ani9, whereas EYFP-QL quenching was either abolished (T16A-inhA01) or statistically significantly reduced (Ani9). This indicates that our imaging approach allows reliable, all-optical measurement of ANO1-mediated CaCCs and concurrent Ca^{2+} dynamics in individual DRG neurons.

TRPV1-ANO1 coupling requires Ca^{2+} release from the ER

ANO1 activation is coupled to intracellular Ca^{2+} release from IP_3Rs in DRG neurons (*19*). To confirm this coupling using our imaging approach, BK was applied in the absence of Ca^{2+} in the extracellular bath solutions (Fig. 2D). The amplitude of EYFP-QL quenching was not affected by the removal of extracellular Ca^{2+} (Fig. 2E), despite a significantly lower induced $[Ca^{2+}]$ rise, compared to control conditions. This finding suggested that although Ca^{2+} influx through PM Ca^{2+} channels contributed to the global Ca^{2+} rises induced by BK (*8*), it was the ER Ca^{2+} release that specifically activated ANO1/CaCC after B_2R activation. As shown previously (*19*), Ca^{2+} influx through VGCCs is poorly coupled to ANO1 activation in DRG neurons. To verify this finding using our imaging approach, we stimulated Ca^{2+} influx through VGCCs by depolarizing neurons with an extracellular solution containing 50 mM KCl (fig. S1, A and B). The majority (15 of 23 or 65%) of DRG neurons did not respond to 50 mM K^+ with any measurable EYFP-QL quenching, despite strong rises in $[Ca^{2+}]_i$. The remaining 35% (8 of 23) of neurons did display quenching (fig. S1, A and B). However, significant EYFP-QL quenching induced by 50 mM KCl was observed in some DRG neurons in the absence of extracellular Ca^{2+} as well (fig. S1, C and D). Because $[Ca^{2+}]_i$ rises were not recorded under these conditions, we conclude that depolarization-induced quenching observed in the minority of DRG neurons was likely not CaCC related. In summary, our data (Fig. 2, A to E, and fig. S1, A to D) established a reliable optical approach for measuring CaCC activation in DRG neurons and confirmed preferential coupling of ANO1/CaCC to IP_3R-mediated Ca^{2+} release from the ER rather than Ca^{2+} influx through PM Ca^{2+} channels in DRG neurons.

TRPV1 activation in DRG neurons and in heterologous expression systems results in activation of ANO1; furthermore, ANO1 potentiates TRPV1-induced depolarization in vitro and the sensory response to heat in vivo (*10*). ANO1 is itself a heat-sensitive channel, with its thermo-sensitivity modulated by Ca^{2+} (*9*). Moreover, both ANO1 and TRPV1 channels are targeted by BK signals (*8*, *19*, *39*). Thus, elucidating the relationships between these two channels may reveal aspects of thermal sensitivity and inflammatory pain mechanisms. Takayama and colleagues suggested that TRPV1 and ANO1 interact physically and that Ca^{2+} influx through TRPV1 is the main mechanism of coupled ANO1 activation (*10*). However, TRPV1 is a nonselective cation channel and, under physiological conditions, conducts mostly Na^+ currents with Ca^{2+} influx contributing only 7 to 10% of the overall current (*30*). On the other hand, TRPV1 activation in DRG neurons induces PLC activation and ER Ca^{2+} release (*31*). Given the coupling of ANO1 to ER-released Ca^{2+}, we used our optical recording approach to test whether this Ca^{2+} source contributed to TRPV1-ANO1 coupling as well. TRPV1 activation with 1 μM capsaicin induced significant EYFP-QL quenching (Fig. 3, A and B), which correlated with intracellular Ca^{2+} rises (Fig. 3A). Both the capsaicin-induced EYFP-QL quenching and Ca^{2+} transients were comparable to those induced by BK (Fig. 3C).

Downloaded from http://stke.sciencemag.org/ on May 3, 2020

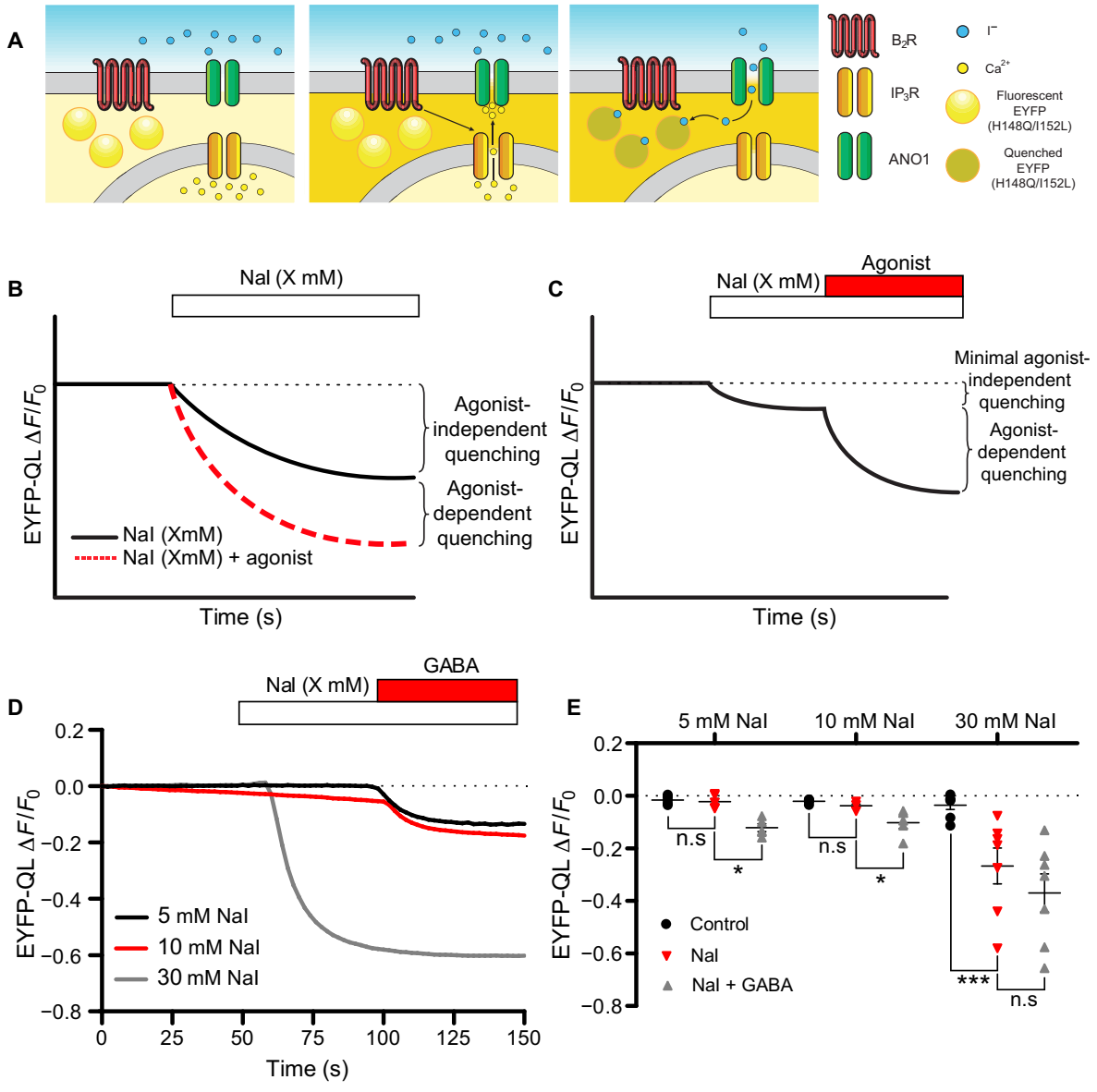

Fig. 1. Optical interrogation of Cl^- channel activity in DRG neurons. (**A**) Schematic of the dual-imaging protocol. DRG neurons are transfected with EYFP (H148Q/I152L); NaI (I^-) is added to the extracellular solutions. Upon stimulation of GPCRs such as the bradykinin receptor B_2R, Ca^{2+} is released from the endoplasmic reticulum (ER) through the IP_3R. This rise in intracellular Ca^{2+} is detected by fura-2 (depicted as brightening of cytosol in the middle and right panels). Activation of ANO1 channels by released Ca^{2+} results in I^- influx, which, in turn, induces quenching of the EYFP-QL fluorescence (right). (**B**) Schematic of expected EYFP (H148Q/I152L) quenching in response to ANO1-mediated I^- influx [30 mM extracellular NaI; based on (*19*)]. (**C**) Schematic of the optimized protocol developed in this study. The concentration of NaI is reduced in steps to develop a protocol with minimal agonist-independent quenching and sufficient dynamic range. (**D**) Representative traces of EYFP (H148Q/I152L) fluorescence quenching produced by 5 (black trace), 10 (red trace), and 30 mM (gray trace) extracellular NaI and subsequently added GABA (100 μM). (**E**) Scatter plots summarizing experiments similar to those shown in (D); 5 mM, $n = 5$ neurons; 10 mM, $n = 5$ neurons; and 30 mM, $n = 7$ neurons. Quenching produced after standard bath solution application (black circles), NaI application (red triangles), and NaI and GABA (100 μM) application (gray triangles). $^*P < 0.05$ and $^{***}P < 0.001$ (paired *t* test); n.s, not significant.

Next, we tested whether Ca^{2+} release from the ER contributed to TRPV1-induced ANO1 activation. As a first step, we measured capsaicin-induced Ca^{2+} transients in untransfected DRG neurons after ER store depletion produced by inhibition of the sarco/ER Ca^{2+}-ATPase (adenosine triphosphatase) by either thapsigargin (TG; 1 μM) or cyclopiazonic acid (CPA; 1 μM; Fig. 3D and fig. S2A). Consistent with a previous report (*31*), Ca^{2+} transients were statistically significantly reduced in the presence of both drugs. However, after removal of Ca^{2+} from the extracellular bath solutions, capsaicin still produced Ca^{2+} signals (Fig. 3D and fig. S2A). These were statistically significantly smaller as compared to control conditions, yet clearly identifiable. These initial experiments indicate that TRPV1 can induce sizeable Ca^{2+} release from the internal stores, which contributes about one-half of the global Ca^{2+} signal measured by fura-2.

Next, we used triple-wavelength imaging to investigate the effect of store depletion on ANO1 activation, as measured with EYFP-QL

Downloaded from http://stke.sciencemag.org/ on May 3, 2020

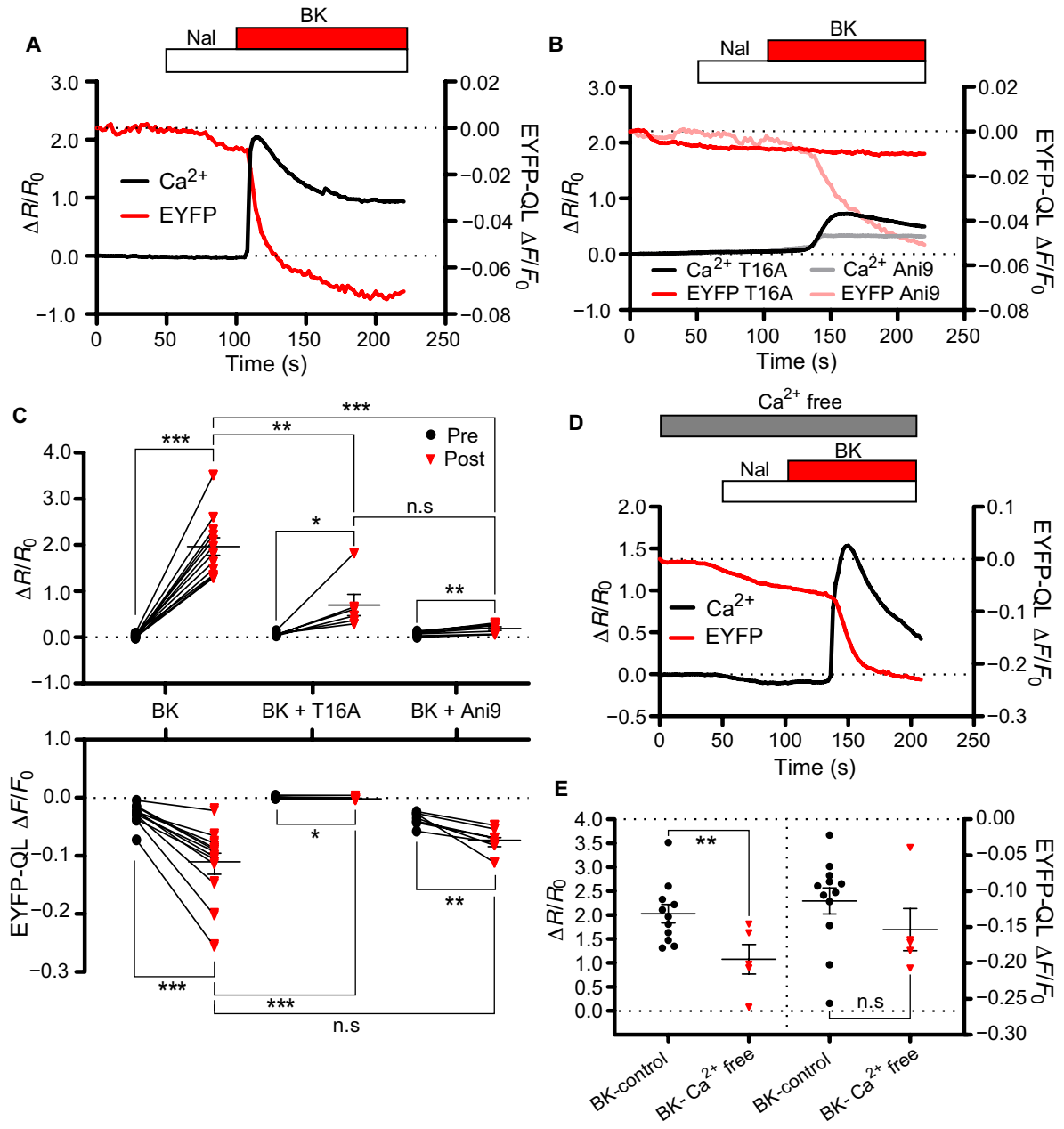

Fig. 2. All-optical demonstration of coupling of CaCC activation to IP_3R-mediated Ca^{2+} release. (**A** and **B**) Representative traces showing Ca^{2+} rises and concurrent EYFP-QL fluorescence quenching in small-diameter DRG neurons transfected with EYFP-QL and loaded with fura-2 AM in response to BK (250 nM) application in the absence (A) or presence (B) of ANO1 inhibitors, T16A-inhA01 (50 μM) or Ani9 (500 nM). (**C**) Scatter plots summarizing experiments similar to those shown in (A) BK ($n = 12$ neurons) and (B) T16A-inhA01 ($n = 6$ neurons) and Ani9 ($n = 7$ neurons). (**D**) Representative traces showing fura-2 and EYFP-QL responses to BK application in DRG neurons when Ca^{2+} was omitted from the extracellular solutions. (**E**) Comparison between the data for BK application with ($n = 12$ neurons) and without extracellular Ca^{2+} ($n = 5$ neurons). In (C) and (E), $^*P < 0.05$, $^{**}P < 0.01$, and $^{***}P < 0.001$ (paired or unpaired t test, as appropriate).

quenching. Depletion of ER Ca^{2+} stores with TG reduced not only Ca^{2+} transients after capsaicin application but also EYFP-QL quenching (fig. S2, B and C). We also applied capsaicin in Ca^{2+}-free extracellular solution and, using our triple-wavelength imaging approach, determined that both Ca^{2+} transients and significant EYFP-QL quenching were still present (fig. S3, A and B). These results provide further support for our proposal that CaCC activation through TRPV1 requires the ER component. We also tested whether ER Ca^{2+} "leak" could induce CaCC activation in our experimental setup. Acute application of TG to EYFP-QL–transfected DRG neurons produced Ca^{2+} transients and some EYFP-QL quenching (fig. S3, C and D).

To further probe the relationship between TRPV1 activation, ER Ca^{2+} release, and ANO1 activation, we expanded our imaging approach to enable simultaneous but separate monitoring of Ca^{2+} levels in the ER and cytosol together with EYFP-QL quenching. To allow ER Ca^{2+} monitoring, we used the ER-targeted, Ca^{2+}-sensing protein red-CEPIA (*40*). CEPIA fluorescence is reduced as Ca^{2+} is released from the ER. We transfected DRG cultures with both EYFP-QL

Downloaded from http://stke.sciencemag.org/ on May 3, 2020

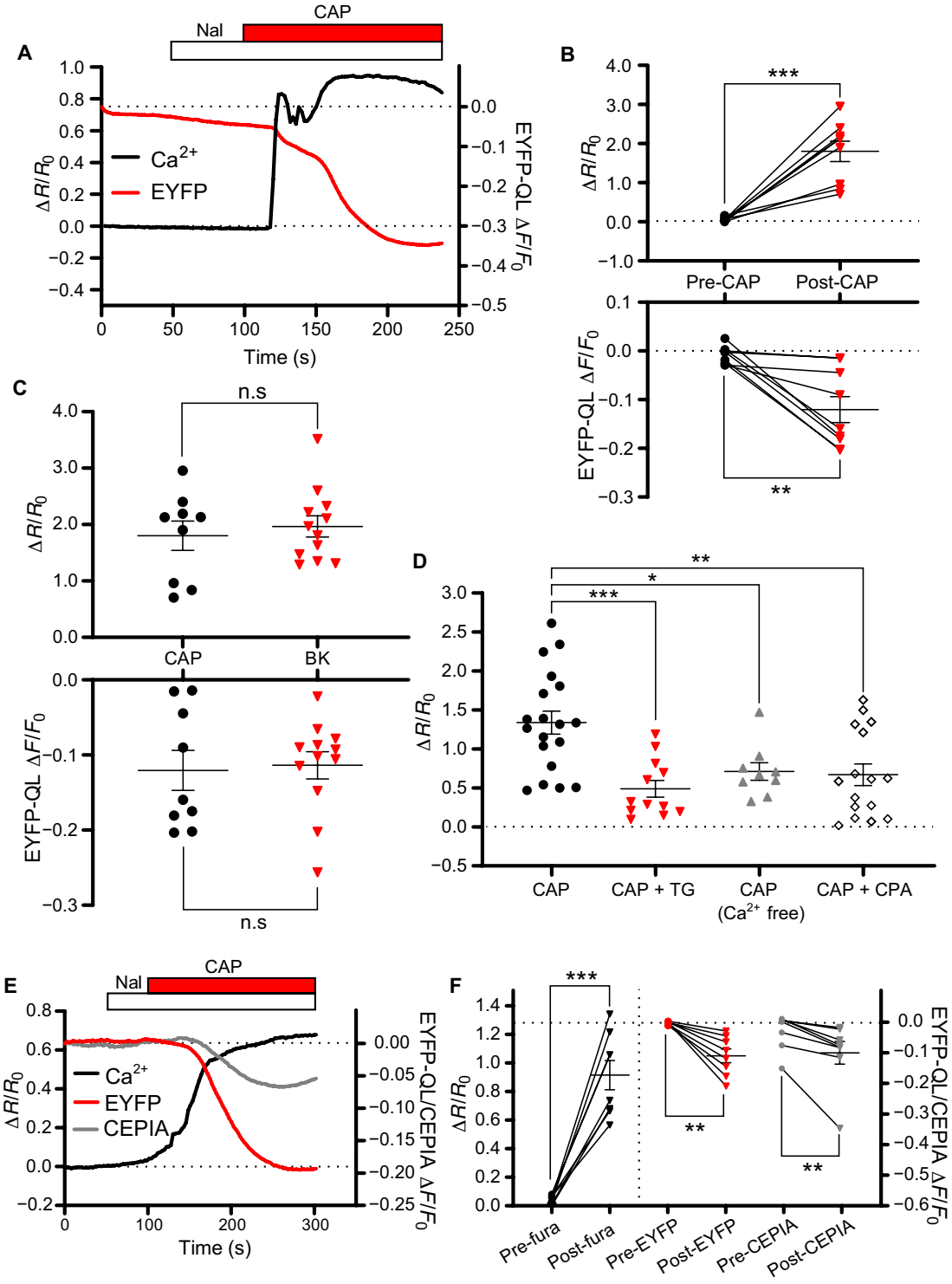

Fig. 3. ER Ca^{2+} release is required for the TRPV1-mediated activation of CaCC. (**A**) Representative traces showing a Ca^{2+} rise and a concurrent EYFP-QL fluorescence quenching in a small-diameter DRG neuron transfected with EYFP-QL and loaded with fura-2 AM in response to capsaicin (1 μM) application. (**B**) Scatter plots summarizing experiments similar to those shown in (A); $n = 9$ neurons. (**C**) Comparisons for the fura-2 ratiometric Ca^{2+} measurement and EYFP-QL fluorescence quenching in response to capsaicin and BK application. (**D**) Summary of fura-2 Ca^{2+} imaging experiments in which capsaicin was applied either under control conditions ($n = 19$ neurons), in the presence of thapsigargin (TG; 1 μM; $n = 12$ neurons), with no extracellular Ca^{2+} ($n = 9$ neurons), or in the presence of cyclopiazonic acid (CPA; 1 μM; $n = 16$ neurons). (**E**) Representative traces showing a response to capsaicin in triple imaging experiments, where fura-2 Ca^{2+} levels (black trace), EYFP-QL fluorescence quenching (red trace), and ER-Ca^{2+} levels using red-CEPIA (gray trace) were simultaneously monitored in EYFP-QL and red-CEPIA cotransfected DRG neurons. (**F**) Scatter plots summarizing experiments similar to those shown in (E), $n = 8$ neurons. In (B) to (F), $^*P < 0.05$, $^{**}P < 0.01$, and $^{***}P < 0.001$ [paired *t* test and Wilcoxon signed-rank test (B) and (F), unpaired *t* test (C), and one-way ANOVA (D)].

Downloaded from http://stke.sciencemag.org/ on May 3, 2020

and red-CEPIA and also loaded cells with fura-2 AM, thereby allowing us to concurrently monitor CaCC activity, ER Ca^{2+} levels, and cytosolic Ca^{2+} dynamics, respectively. A quadruple-wavelength (340/380/488/560 nm) imaging protocol was used to simultaneously image all fluorophores in the experiments. Application of capsaicin not only produced Ca^{2+} transients and evoked significant EYFP-QL quenching but also resulted in a reduction in red-CEPIA fluorescence, which indicates Ca^{2+} moving out of the ER after TRPV1 activation (Fig. 3, E and F). This experiment also directly demonstrated good temporal correlation between ER Ca^{2+} depletion, cytosolic Ca^{2+} elevation, and CaCC activation.

To validate our imaging results, we made whole-cell patch-clamp recordings from cultured DRG neurons using physiological bath and internal pipette solutions. Application of capsaicin elicited robust inward currents (Fig. 4A). The current amplitude and kinetics of the response varied substantially; therefore, we quantified the area under the curve (A.U.C.) as a readout of TRPV1 activation. To test the contribution of ANO1 to this current, DRG neurons were preincubated with Ani9 (500 nM; Fig. 4A). In the presence of Ani9, the capsaicin-induced A.U.C. was statistically significantly reduced, which was consistent with a previous study (*10*). To test whether Ca^{2+} release from the ER was necessary for TRPV1-coupled ANO1 activation in DRG neurons, we pretreated neurons with TG (1 μM), which significantly reduced the capsaicin-induced A.U.C. (Fig. 4, B and C). In the presence of TG, most of the responses to capsaicin were lower compared to those evoked in control conditions [Fig. 4, B (black trace) and C]. However, in five TG-treated neurons, capsaicin-induced responses were within the range of the average capsaicin response under control conditions [Fig. 4, B (red trace) and C]. These results suggested three conclusions. First, ANO1-mediated Cl^- current contributed substantially to the macroscopic currents induced in DRG neurons by capsaicin. Second, TRPV1-induced release of Ca^{2+} from the ER contributed substantially to TRPV1-coupled ANO1 activation in most of DRG neurons. Third, in some neurons, TRPV1-mediated Ca^{2+} influx was sufficient to induce strong ANO1 activation. The latter observation also argues against the possibility that TG directly interferes with TRPV1 function.

TRPV1-mediated Ca^{2+} release from the ER requires cross-talk between plasmalemmal TRPV1 and PLC

One important question that needed to be addressed was the manner in which capsaicin activated ER Ca^{2+} release. The two most likely scenarios suggested in the literature are activation of PLCs that cleave phosphatidylinositol 4,5-bisphosphate (PIP_2) to produce IP_3, which, in turn, induces Ca^{2+} release through IP_3Rs in the ER (*41*), and direct activation of ER-localized TRPV1 channels by capsaicin (*42*). To differentiate between the above mechanisms, we used two approaches. First, we performed fluo-4 Ca^{2+} imaging in DRG neurons treated with capsaicin after preincubation with (and in the presence of) ruthenium red (RR; 10 μM), a cell-impermeable TRPV1 blocker (Fig. 5, A and B). Without access to the cytosol, RR should not inhibit putative ER-localized TRPV1 channels; therefore, capsaicin responses in the presence of this TRPV1 blocker could be attributed to this subset of channels (or any other intracellular TRPV1 channel pool). There was generally no response to capsaicin in the presence of RR (Fig. 5, A and B). Upon washout of RR and with capsaicin still present, Ca^{2+} responses were routinely recorded, suggesting that capsaicin did not induce noticeable Ca^{2+} transients through putative ER-resident TRPV1 channels in most of DRG neurons under our experimental conditions.

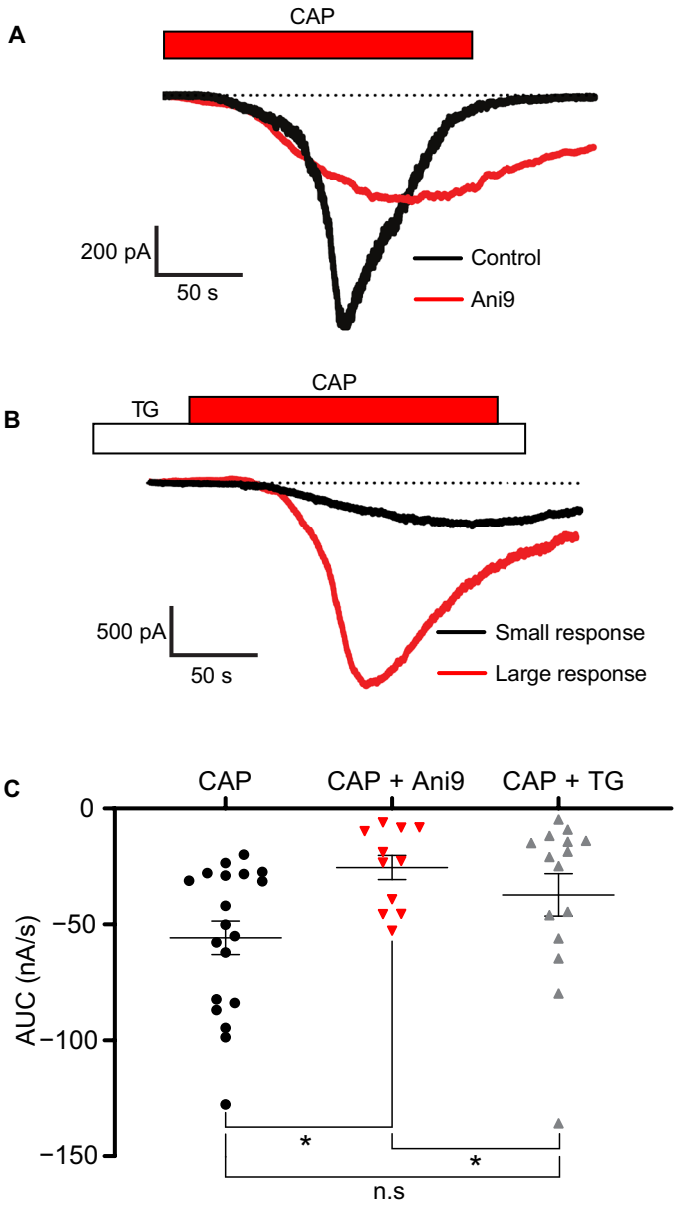

Fig. 4. TG disrupts capsaicin-induced currents in small-diameter DRG neurons. (**A**) Representative whole-cell patch-clamp recordings from DRG neurons held at −60 mV during application of capsaicin (1 μM) in the absence (black trace) or presence (red trace) of the ANO1 inhibitor Ani9 (500 nM). (**B**) Responses to capsaicin (1 μM) in the presence of TG (1 μM). Capsaicin-induced currents that were smaller (black trace) or of comparable amplitude (red trace) to those obtained under control conditions are shown. (**C**) Scatter plots summarizing areas under the curve for capsaicin responses in experiments similar to these shown in (A) and (B); control (n = 18 neurons), Ani9 (n = 11 neurons); TG (n = 16 neurons). In (C), *P < 0.05 (Kruskal-Wallis ANOVA with Mann-Whitney test).

Of 38 neurons that responded to capsaicin upon RR washout, only four cells produced discernable Ca^{2+} transients in the presence of RR and capsaicin. To specifically probe ER-Ca^{2+} release by TRPV1 activation, we performed imaging in DRG neurons expressing green-CEPIA to enable direct monitoring of ER Ca^{2+} levels. Capsaicin application produced significant ER depletion only after RR washout (Fig. 5, C and D).

Downloaded from http://stke.sciencemag.org/ on May 3, 2020

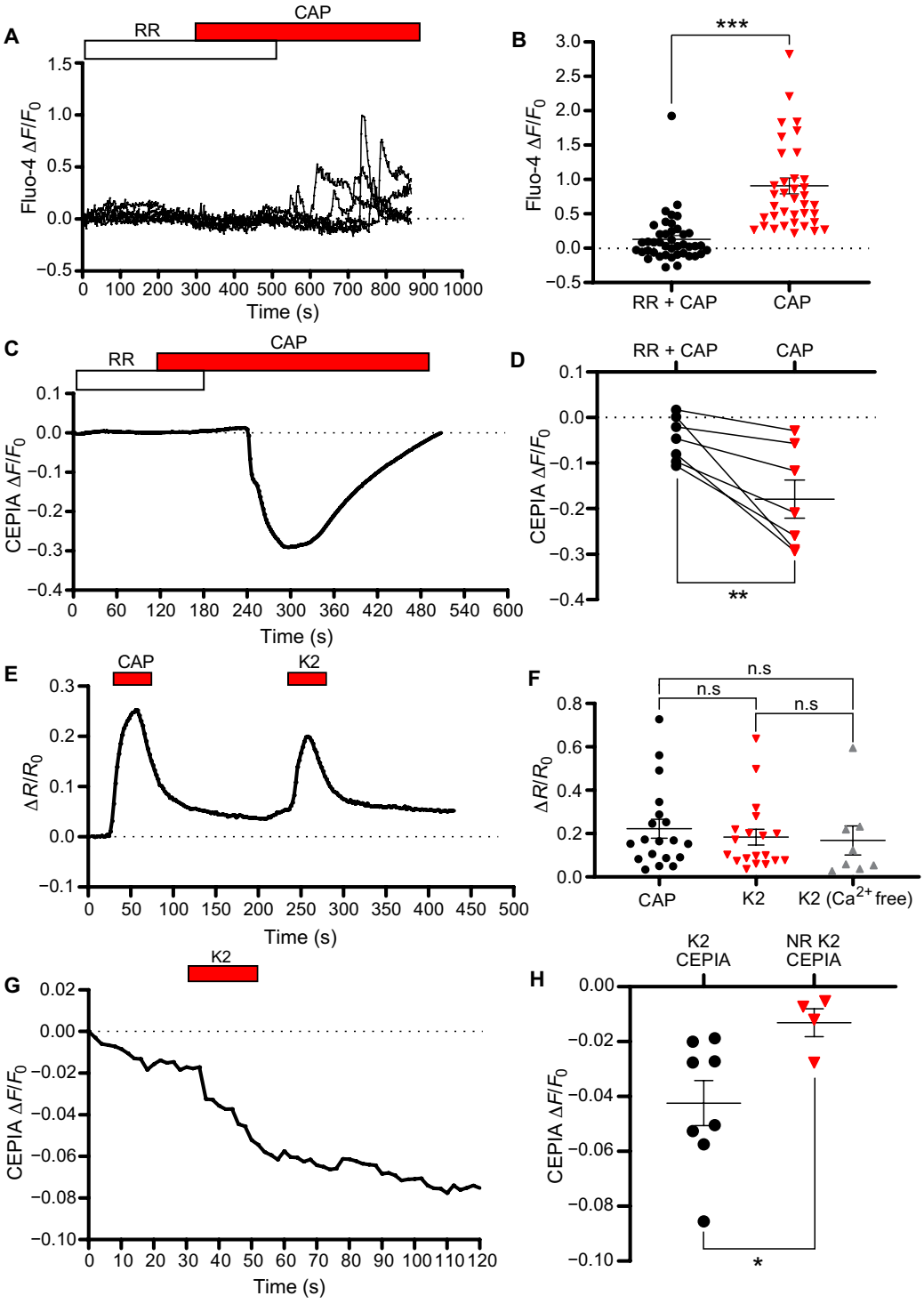

Fig. 5. ER-localized TRPV1 channels are not engaged during extracellular TRPV1 stimulation in small-diameter DRG neurons. (**A**) Representative traces showing Ca^{2+} responses in small-diameter DRG neurons loaded with fluo-4 AM in response to capsaicin (1 μM) in the presence of ruthenium red (RR; 10 μM) and after the RR washout. (**B**) Scatter plots summarizing experiments similar to those shown in (A); RR + CAP ($n = 42$ neurons); CAP ($n = 38$ neurons). (**C**) Representative trace showing fluorescence changes in small-diameter DRG neurons transfected with green-CEPIA in response to capsaicin (1 μM) in the presence of RR (10 μM) and after the RR washout. (**D**) Scatter plots summarizing experiments similar to those shown in (C); $n = 6$ neurons. (**E**) Representative traces showing a Ca^{2+} response in a small-diameter DRG neuron loaded with fura-2 AM in response to capsaicin (1 μM) and K2 (30 μM). (**F**) Scatter plots summarizing experiments similar to those shown in (E); CAP, $n = 19$ neurons; K2, $n = 19$ neurons; K2 (Ca^{2+} free), $n = 8$ neurons. (**G**) Representative trace showing fluorescence changes in a small-diameter DRG neuron transfected with red-CEPIA in response to K2 (30 μM). (**H**) Scatter plots summarizing experiments similar to those shown in (G); K2 CEPIA, responding neurons ($n = 8$ neurons); NR K2 CEPIA, non-responding neurons ($n = 4$ neurons). In (B), (D), (F), and (H), $^*P < 0.05$, $^{**}P < 0.01$, and $^{***}P < 0.001$ [Mann-Whitney test (B), paired t test (D), Kruskal-Wallis ANOVA with Mann-Whitney test (F), and unpaired t test (H)].

Downloaded from http://stke.sciencemag.org/ on May 3, 2020

Second, we used a cell-impermeable TRPV1 ligand to specifically activate PM-resident TRPV1 channels while avoiding activation of intracellular TRPV1s. Double-knot toxin (DkTx) is a vanillotoxin from the Chinese bird spider (*Ornithoctonus huwena*) which activates TRPV1 by binding to its extracellular outer pore turret (*43*–*45*). Here, we used a single-knot derivative of DkTx, K2, which activates TRPV1 with improved efficacy (*46*). Both capsaicin and K2 (30 μM) evoked comparable Ca^{2+} transients in DRG neurons (Fig. 5, E and F). In the absence of Ca^{2+}, K2 still induced cytosolic Ca^{2+} transients (Fig. 5F and fig. S4). Last, DRG cultures were transfected with red-CEPIA, and K2 was applied to test whether Ca^{2+} release from the ER could be detected. K2 induced significant reduction in CEPIA fluorescence in 8 of 12 neurons tested (Fig. 5, G and H). The data obtained with both a cell-impermeable TRPV1 agonist and a cell-impermeable antagonist suggested that activation of PM-localized TRPV1 channels was capable of inducing Ca^{2+} release from the ER. Contribution of putative ER-localized TRPV1 channels to the capsaicin-induced cytosolic Ca^{2+} signal in DRG neurons appeared to be negligible.

The alternative possibility is that TRPV1 activation in DRG neurons was coupled to PLC activation and subsequent Ca^{2+} mobilization (*31*). To test this possibility, we transfected DRG neurons with an optical PIP_2 reporter, green fluorescent protein (GFP)–tagged plextrin homology domain of PLCδ (PLCδ-PH-GFP), and monitored its translocation from the membrane to cytosol following the capsaicin application as a measure of PIP_2 hydrolysis by PLC (*47*). Application of capsaicin (1 μM) induced translocation of PLCδ-PH-GFP from the PM to the cytosol (fig. S5, A and B). Translocation was recorded even in the absence of extracellular Ca^{2+}, albeit to a smaller extent (fig. S5B). Both of these findings are consistent with the previous report (*31*) and with our K2 experiments.

ANO1, TRPV1, and IP_3R cluster at ER-PM junctions

Our results above suggested that there were functional interactions between ANO1, TRPV1, and IP_3Rs that allowed TRPV1 to activate ANO1 through IP_3R-mediated Ca^{2+} release, supplementing the relatively small Ca^{2+} influx through TRPV1 itself (*30*). For this mechanism to occur, there must be close proximity between these channel proteins. Previous work suggests that at least some ANO1 channels in DRG neurons reside at ER-PM junctions (*1*, *19*), which are sites for intracellular information transfer where two membrane types come into very close juxtaposition (~15 nM) (*48*). At these sites, ANO1 channels may physically interact with the IP_3Rs (*19*, *49*). To test whether all three proteins were found in close association, we first used a proximity ligation assay (PLA), which detects two proteins that are closer than 30 to 40 nm from each other by manifesting characteristic 0.5 to 1 μm fluorescent puncta (*50*, *51*). All antibodies used for PLA have been previously validated extensively by us in sensory neurons (*19*, *52*).

Specific PLA signals indicating close proximity were detected for TRPV1-ANO1 (Fig. 6A), ANO1-IP_3R1 (Fig. 6B), and TRPV1-IP_3R1 (Fig. 6C) protein pairs. A particularly high concentration of puncta per neuron was observed for the TRPV1-ANO1 pair (Fig. 6D). Positive PLA controls using two primary ANO1 antibodies raised in rabbit and goat and corresponding secondary PLA probes displayed robust puncta (fig. S6A). When only the rabbit primary antibody was used with both secondary probes, no signal was detected (fig. S6B). No puncta were observed when PLA was performed between IP_3R1 and CD71 (also known as the transferrin receptor) (fig. S7A), a nonraft plasmalemmal protein (*19*, *53*) that is not expected to colocalize with the members of the ANO1 junctional complex (*19*). These controls confirm PLA specificity in our experimental settings. Together, these data established that ANO1, TRPV1, and IP_3R1 in DRG neurons often are found in close proximity. Of the three pairs tested, TRPV1-ANO1 complexes were more easily detectable, perhaps reflecting the PM residence of these proteins, whereas ANO1-IP_3R1 and TRPV1-IP_3R1 interactions exist across the ER-PM junction.

STORM superresolution microscopy allows direct visualization of individual ANO1-TRPV1-IP_3R complexes

To further probe the existence of multichannel complexes suggested by the above data with greater precision, we used multiwavelength superresolution microscopy that can detect individual protein molecules in the membrane of fixed primary cells. Stochastic optical reconstruction microscopy (STORM) (*54*, *55*) allows multiple fluorophore excitation and detection using visible light, enabling localization of individual proteins, or complexes within a lateral resolution of less than 50 nm (*52*). Our previous work (*52*) describes in detail the extensive controls performed for such multiwavelength STORM and the analysis paradigms that we have developed. The traditional STORM approach incorporates different "activator" fluorescent dyes (in this work, we used Alexa Fluor 405, Cy2, and Cy3, excited at 405, 488, or 561 nm, respectively) that excite a common "reporter" fluorescent dye (for example, Alexa Fluor 647), which are both conjugated to secondary antibodies to identify which activator dye is the source of the excitation signal through tight temporal correlation. Each protein of interest is first labeled with appropriate primary antibodies that we have validated previously (*19*, *52*). Because each secondary antibody is specific to the species of a corresponding primary antibody (mouse, rabbit, and goat), we can simultaneously visualize individual complexes containing up to three different proteins. Control experiments by our group have shown a single tetrameric ion channel (such as voltage-gated K^+ channel or a TRP channel) to be represented by a cluster of labeled "centroids" (single-molecule localizations) with a radius of ~30 to 50 nm, in which a single type of protein is represented by a cluster of densely proximal, like-colored centroids (*52*). Complexes containing two or three types of physically associated proteins are represented by clusters of centroids of two or three colors, with a slightly greater radial "footprint" of the antibody dye label (*52*). Each standalone cluster of centroids of a single color represents a protein or a complex (such as a multimeric ion channel), recognized by a single type of a primary antibody. Clusters of centroids are objectively identified with a density-based spatial clustering of applications with noise (DBSCAN) algorithm based on the original STORM localization data, which we previously described. Differential bleaching kinetics of Alexa Fluor 405, Cy2, and Cy3 (fig. S8) were corrected.

First, we used STORM to probe for the same combinations of protein complexes tested in the PLA experiments (TRPV1-ANO1, ANO1-IP_3R1, and TRPV1-IP_3R1; Fig. 7, A to C). Clusters of centroids representing individual ANO1, TRPV1, and IP_3R1 channels were detected in each corresponding experiment, and as expected, a fraction of these centroid clusters were comingled within a combined radius of <120 nm, indicating close association. Even when in tight proximity (<100 nm), the footprint of each channel protein, as labeled by the STORM-visualized antibody/dyes, could be individually resolved from the associated, coupled protein (Fig. 7, A to C). Of the total detected clusters of centroids for TRPV1 and ANO1, 74.1 ± 6.5% were identified as colocalized channels based on our analysis paradigm

Downloaded from http://stke.sciencemag.org/ on May 3, 2020

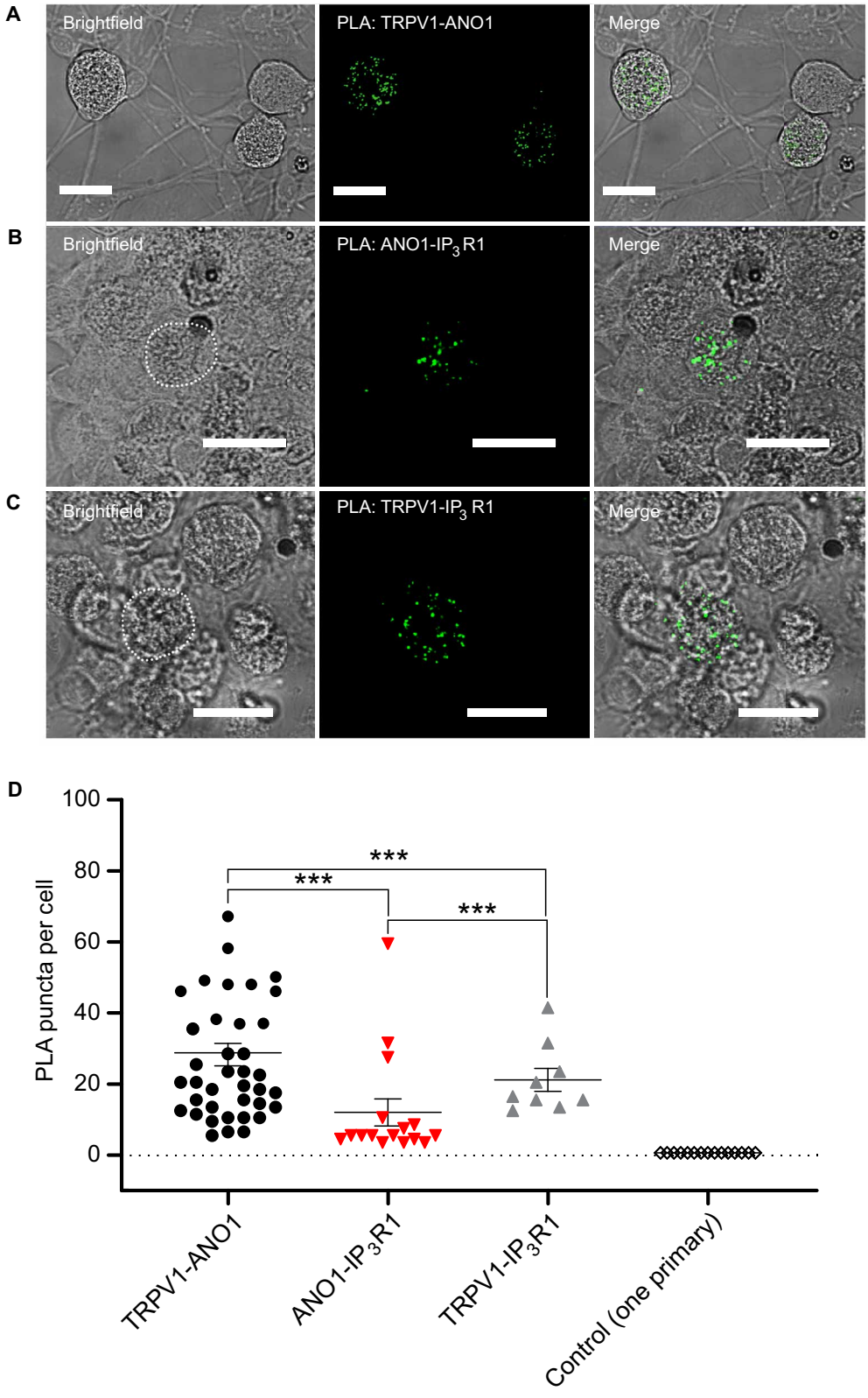

Fig. 6. ANO1, TRPV1, and IP_3R1s are in close proximity in small-diameter DRG neurons as tested with proximity ligation assay. (**A** to **C**) PLA images for TRPV1-ANO1 (A), ANO1-IP_3R1 (B), and TRPV1-IP_3R1 (C) pairs in DRG cultures. Left, brightfield images; middle, PLA puncta detection; right, merged images of brightfield and PLA puncta. Scale bars, 20 μm. (**D**) Scatter plots summarizing number of PLA puncta per cell in experiments similar to these shown in (A) to (C); TRPV1-ANO1 (n = 41 neurons), ANO1-IP_3R1 (n = 16 neurons), and TRPV1-IP_3R1 (n = 16 neurons); black outlined symbols depict negative control where only one primary antibody (against ANO1) was used in conjunction with both PLA secondary probes (fig. S6, A and B). In (D), ***P < 0.001 (Kruskal-Wallis ANOVA with Mann-Whitney test).

Downloaded from http://stke.sciencemag.org/ on May 3, 2020

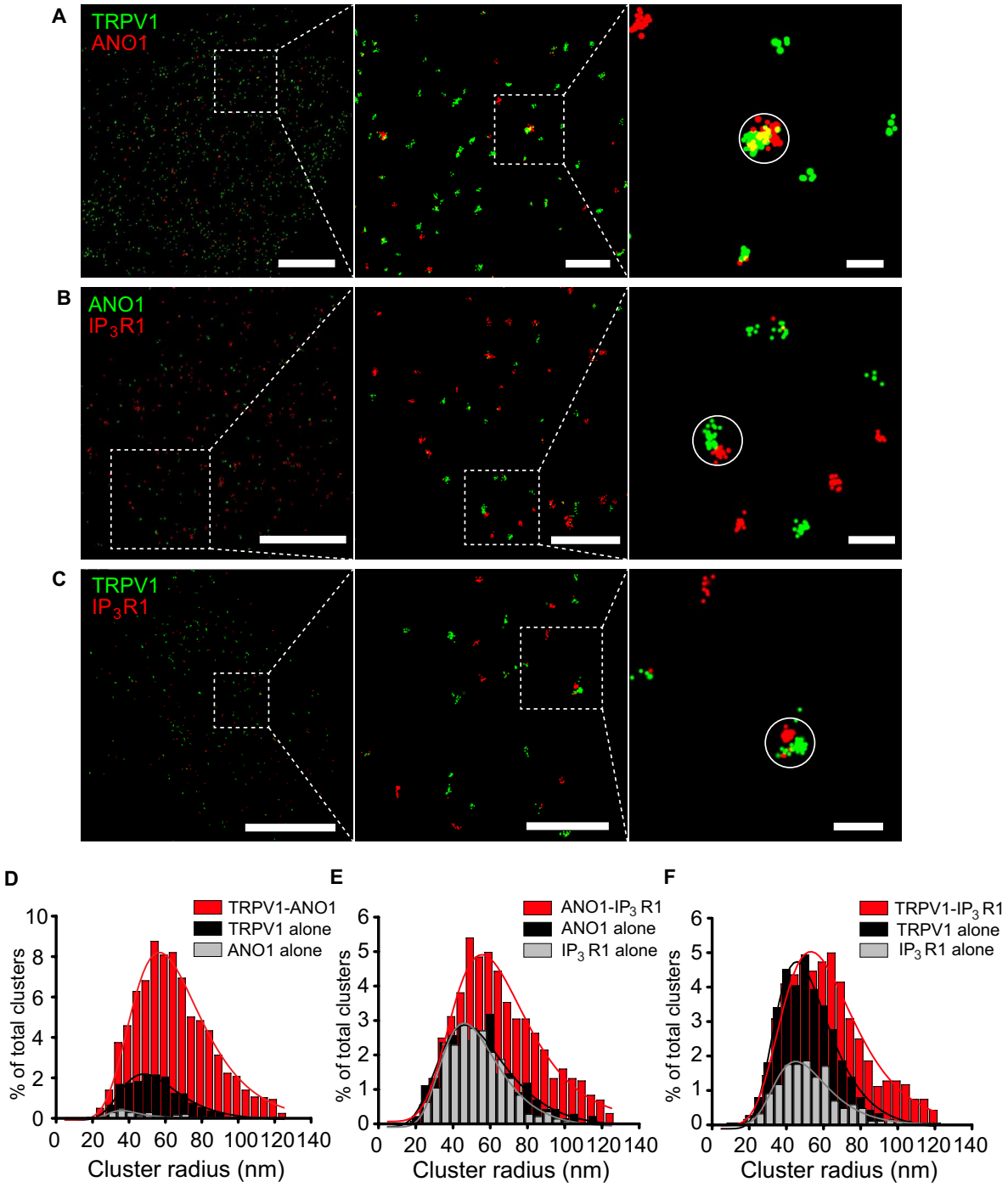

Fig. 7. ANO1, TRPV1, and IP$_3$R1s are found in close proximity in small-diameter DRG neurons as tested with STORM. (**A** to **C**) Right panels display representative STORM images from DRG neurons, double-labeled for either TRPV1 and ANO1 (A), ANO1 and IP$_3$R1 (B), or TRPV1 and IP$_3$R1 (C) using dye pairs of Alexa Fluor 405/Alexa Fluor 647 (green centroids) and Cy3/Alexa Fluor 647 (red centroids); scale is indicated by the white bars; 5 μm (left), 1 μm (middle), and 0.2 μm (right) for (A) to (C). (**D** to **F**) Cluster distributions representing double-labeled TRPV1-ANO1, $n = 6$ neurons (D); ANO1-IP$_3$R1, $n = 9$ neurons (E); or TRPV1-IP$_3$R1, $n = 6$ neurons (F). Summary data for cluster percentages, localization number per cluster, and probability distribution statistics are given in tables S1 to S3.

(Fig. 7D) (*52*). The observed overlap of the two channels (as represented by their respective like-colored centroid clusters) in two-dimensional (2D) space in the STORM image was usually not complete, suggesting discrete channels that were physically coupled in the PM within very close proximity. Non-colocalized ANO1 (2.3 ± 0.5%) and TRPV1 channels (23.5 ± 6.4%) were also detected, which were a lower fraction compared to the colocalized population (table S1).

In our experiments, STORM was performed on a microscope platform similar to that of total internal reflection fluorescence microscopy, in which illumination of cells is typically restricted to

Downloaded from http://stke.sciencemag.org/ on May 3, 2020

<400 nm from the surface of the glass, with the bulk of the light internally reflected (*56*, *57*). In STORM, the angle of the laser light can be altered so that the illumination is not fully internally reflected, but adjusted so it is sufficiently oblique to penetrate up to ~1 μm, allowing illumination of the cytosol or organelles (such as the ER membrane) within 1 μm of the PM. Thus, we used STORM to examine the presence of complexes containing individual TRPV1 or ANO1 channels in the PM and closely proximal to ER-resident IP_3Rs. In double-labeling of ANO1 and IP_3R1 under STORM, we detected colocalized ANO1-IP_3R1 complexes, represented by clusters of centroids of two colors, accounting for 54.2 ± 4.3% of all detected centroid clusters observed in DRGs (Fig. 7E). Clusters of centroids of a single color, representing individual ANO1 channels or IP_3R1s comprised 23.8 ± 4.0% and 22.0 ± 8.1% of all clusters, respectively. We also probed for complexes containing TRPV1 and IP_3R1 and found colocalization of the two proteins, accounting for 51.8 ± 4.0% of detected clusters (Fig. 7F). Individual TRPV1 and IP_3R1 clusters amounted to 34.0 ± 4.0% and 14.1 ± 0.8% of total clusters, respectively (table S1). As with the PLA data, the fraction of total TRPV1-ANO1 complexes per cell was more abundant as compared to complexes containing ANO1-IP_3R1 or TRPV1-IP_3R1. Although this cross-comparison of protein pairs (both by STORM and PLA) suggests the colocalization of ANO1, TRPV1, and IP_3R1 that we can visualize, it does not provide quantitative evidence for the relative abundance of individual pairs, because the primary antibody affinities to their respective epitopes are not uniform and cannot be meaningfully normalized.

Because the PLA approach is limited to the detection of protein pairs only, we performed triple-labeled STORM imaging to probe for complexes containing all three proteins (ANO1, 405/647; TRPV1, 488/647; IP_3R1, 561/647; Fig. 8, A to C). The fraction of ANO1, TRPV1, and IP_3R1 detected as colocalized together was 40.2 ± 0.2%, which accounted for the majority of the colocalizations compared to the pairs of only TRPV1-ANO1 (15.7 ± 1.6%), ANO1-IP_3R1 (4.2 ± 0.04%), and TRPV1-IP_3R1 (6.4 ± 1.6%) without a third protein observed (table S1). The ANO1-IP_3R1–only and TRPV1-IP_3R1–only populations were small and under the noise threshold of interactions detectable under STORM that we previously determined. This "noise threshold" was experimentally determined as ~10% of total clusters (based on spurious interactions of KCNQ2 and KCNQ4 channels) and in which the binned cluster radii are consistently less than 1% of the total fraction of clusters (*52*). Clustering between IP_3R1 and CD71 amounted to 10.6 ± 1.6% of total clusters (fig. S7B), confirming the stringency of our threshold criteria and agreeing with the PLA results (fig. S7A).

In triple-labeled cells, TRPV1-ANO1 colocalizations remained prevalent, consistent with the large number of physical interactions of these two PM proteins in the double-label STORM experiments. However, the mean radius and centroid density of the ANO1-TRPV1-IP_3R1 clusters were statistically significantly larger than these of the TRPV1-ANO1 (no IP_3R1) clusters, presumably because of the addition of the IP_3R1s (tables S2 and S3). This is important when comparing these data to the double-labeled STORM experiments, in which the cluster populations of colocalized pairs of proteins were similar in size and centroid density (tables S2 and S3). On the basis of the proportion of complexes, we can surmise that ANO1 and TRPV1 are more likely to cluster in the presence of colocalized IP_3R1, as evident in the statistically significantly greater number of triple-color clusters including IP_3R1s.

DISCUSSION

In this work, we investigated the mechanism coupling TRPV1 channel opening with the activation of ANO1/CaCC in small-diameter (presumed nociceptive) DRG neurons. In the original report of TRPV1-ANO1 interactions, Takayama and colleagues put forward the most straightforward explanation for the mechanism of coupling: opening of the TRPV1 channel pore delivers a sufficient amount of Ca^{2+} to directly activate colocalized ANO1 channels (*10*). Yet, several considerations compelled us to look beyond Occam's razor. First, the affinity of Ca^{2+} ions for ANO1 at negative voltages is low [2 to 5 μM (*7*, *13*)]. Second, the Ca^{2+} current fraction amounts to no more than 10% of the macroscopic TRPV1 current under physiological conditions (*30*). This means that at similar whole-cell current amplitudes (at typical voltages during stimulation), the TRPV1-mediated Ca^{2+} influx would only deliver a fraction of Ca^{2+} ions to the cytosol as compared to those through VGCCs; however, even the latter source alone is not sufficient to produce strong ANO1 activation in DRG neurons [(*19*); present study]. Third, evidence exists suggesting that the ER store refilling Ca^{2+} release–activated channel (CRAC) in *Xenopus* oocytes is indirectly coupled to ANO1 activation. Ca^{2+} entering the cytosol through CRAC is not sufficient to activate ANO1 due to lack of close proximity between the ANO1 and CRAC. Instead, this cytosolic Ca^{2+} is first pumped into the ER by the SERCA pump (sarco/endoplasmic reticulum Ca^{2+}-ATPase) and then released through the IP_3Rs onto the juxtaposed ANO1 channels to produce activation of the latter (*58*). Last, TRPV1 activates Ca^{2+}-sensitive PLCδ and induces subsequent Ca^{2+} release from the ER through IP_3Rs in DRG neurons and expression systems (*31*, *59*). Thus, there might be both the need and a mechanism for more focused delivery of Ca^{2+} to ANO1 channels to ensure robust TRPV1-ANO1 coupling.

Here, using various approaches, we investigated the mechanism of localized Ca^{2+} signals linking ANO1 channel activation to TRPV1 in DRG neurons. First, we confirmed previous observations regarding the coupling of ANO1 to Ca^{2+} sources in DRG neurons: ANO1 can be reliably activated by G_qPCR-induced Ca^{2+} release from the ER (Fig. 2, A, D, and E) (*7*, *19*, *49*) and by Ca^{2+} transients downstream of TRPV1 activation (Fig. 3, A to F) (*10*), whereas Ca^{2+} influx through VGCCs is poorly coupled to ANO1 activation (fig. S1, A and B) (*19*).

We also discovered that the predominant source of Ca^{2+} for TRPV1-coupled ANO1 activation is, as in the case with G_qPCRs, release of Ca^{2+} from the ER. ER store depletion significantly reduced capsaicin-induced Ca^{2+} transients (Fig. 3D) and CaCC activation (Fig. 4B and fig. S2, B and C). In support of the conclusion that TRPV1 is capable of inducing robust Ca^{2+} release from the ER, we demonstrated that capsaicin-induced depletion of ER $Ca^{2+}$was temporally correlated with the rise in cytosolic Ca^{2+} levels and CaCC activation in DRG neurons (Fig. 3, E and F). Capsaicin still produced small Ca^{2+} transients in the absence of extracellular Ca^{2+} (Fig. 3D and fig. S2A), which could be explained by the presence of some functional TRPV1 channels within the ER membrane (*60*). Such a mechanism could also contribute to coupling of ER Ca^{2+} release to ANO1 activation. However, using cell membrane–impermeable manipulators of TRPV1 activity, we showed that inhibition of PM-resident TRPV1 channels prevented capsaicin from producing cytosolic Ca^{2+} transients and ER store depletion (Fig. 5, A to D). Moreover, activation of PM-resident TRPV1 channels produced Ca^{2+} transients even in the absence of extracellular Ca^{2+} and also induced ER store depletion (Fig. 5, E to H, and fig. S4). Hence, PM-resident TRPV1 channels must be coupled to ER Ca^{2+} stores through intracellular signaling mechanisms. To probe this, we demonstrated that TRPV1

Downloaded from http://stke.sciencemag.org/ on May 3, 2020

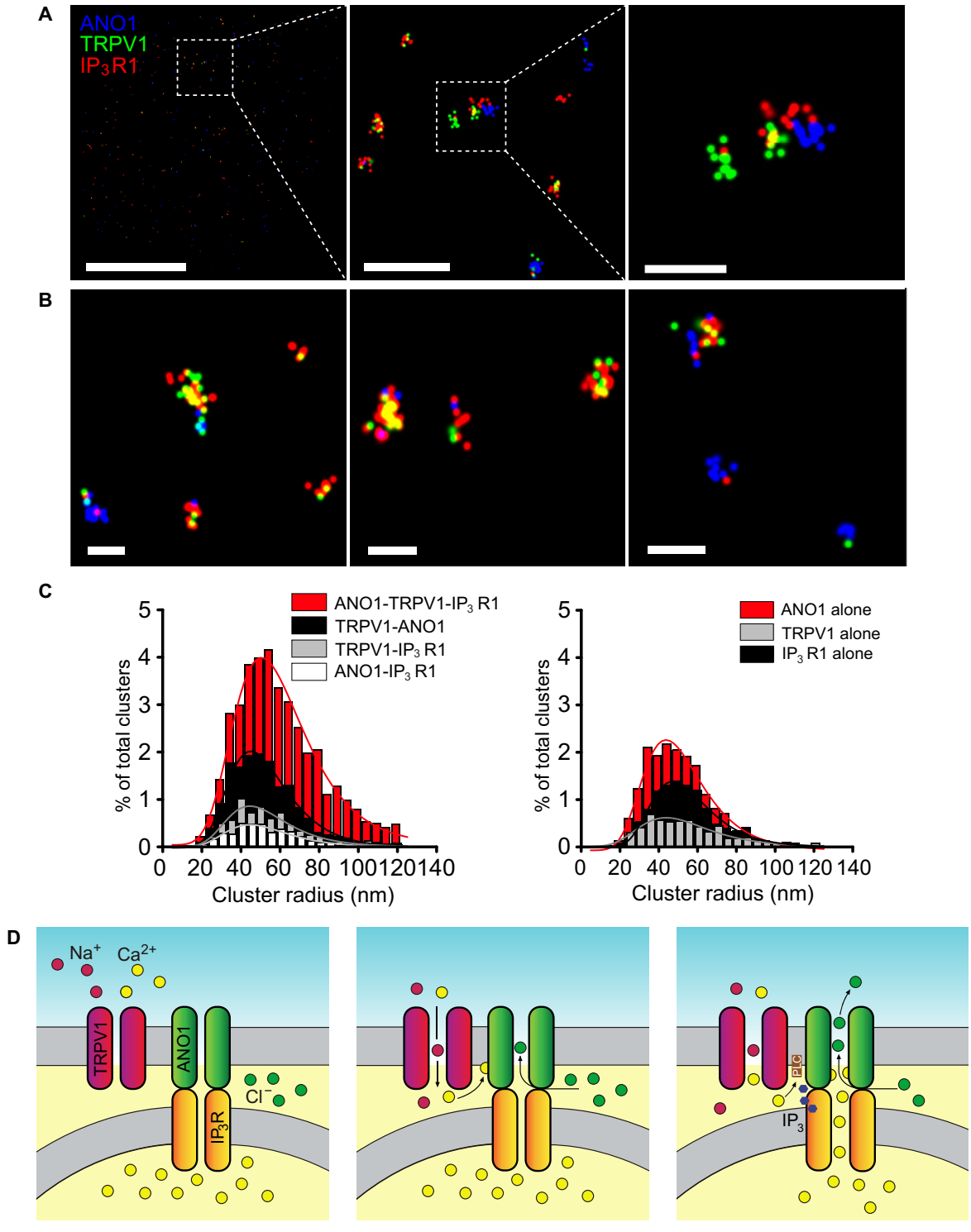

Fig. 8. Imaging of ANO1-TRPV1-IP$_3$R1 complexes using three-color STORM. (**A** and **B**) Representative STORM images for triple-labeled ANO1 (blue centroids), TRPV1 (green centroids), and IP$_3$R1 (red centroids) in DRG neurons; scale is indicated by the white bars; 5 μm (left, A), 1 μm (middle, A), 0.2 μm (right, A), and 0.2 μm (for all images, B). (**C**) Cluster distributions representing triple-labeled ANO1-TRPV1-IP$_3$R1 combinations of proteins, protein pairs, or single proteins; n = 12 neurons. Summary data for cluster percentages, localization number per cluster, and probability distribution statistics are given in tables S1 to S3. (**D**) Schematic depicting possible ANO1-TRPV1-IP$_3$R1 functional coupling in DRG neurons. Our data suggest that a sizable fraction of ANO1, TRPV1, and IP$_3$R1s are in close proximity at the ER-PM junctions and form complexes in small-diameter DRG neurons. TRPV1 activation not only leads to Na^+ and Ca^{2+} influx (middle) but can also activate IP$_3$R Ca^{2+} release (right), presumably through PLC activation. Release of Ca^{2+} from the ER maximizes ANO1 activation (right), which ultimately causes Cl^- efflux and depolarization of the neuron.

Downloaded from http://stke.sciencemag.org/ on May 3, 2020

activation induced acute PIP_2 hydrolysis not only in the presence of extracellular Ca^{2+} but also in extracellular Ca^{2+}-free conditions [albeit less robust in the latter case (fig. S5, A and B)]. These observations agree with a previous study (*31*). The most obvious mechanism for TRPV1-induced ER store release is stimulation of the Ca^{2+}-dependent PLCδ postulated earlier (*31*, *59*). Some degree of capsaicin-induced ER store depletion observed in extracellular Ca^{2+}-free conditions is intriguing because it points toward the existence of additional, hitherto unknown mechanism of coupling, perhaps involving other PLC isoforms. Identifying this mechanism will require further investigation. Yet, under physiological conditions, the Ca^{2+}-dependent PLCδ mechanism of IP_3 generation triggered by the Ca^{2+} influx through the TRPV1 channels is likely to be the dominant one.

Our PLA and STORM experiments revealed that a statistically significant fraction of ANO1, TRPV1, and IP_3R channels assemble into complexes containing two of the three, or all three together, with those containing IP_3Rs located at ER-PM junctional nanodomains. At such junctions, B_2Rs, ANO1 (*1*, *19*, *61*, *62*), and TRPV1 channels (*63*) are likely anchored within caveolin-1–rich lipid rafts at the PM side of the junction, whereas IP_3Rs at the ER are juxtaposed to ANO1. Using triple-label STORM, we identified the populations of each protein complex containing a combination of ANO1, TRPV1, and IP_3Rs (Fig. 8, A to C). Our imaging conditions provided the ability to examine ER-localized IP_3Rs that are proximal to the PM, but we also observed a small percentage of labeled IP_3R1s (11%) that were not colocalized with ANO1 or TRPV1 channels. On the basis of the proximity analysis of ANO1 and TRPV1 colocalizations, there was a statistically significantly greater likelihood that these channels are also in nanodomain clusters with IP_3R1s, compared to TRPV1-ANO1 clusters without close proximity to IP_3R1. However, not all TRPV1-ANO1 complexes were found being associated with IP_3Rs; this may indicate a separate, direct coupling between TRPV1 and ANO1. Thus, we conclude, on the basis of our functional data, that it is likely that not all ANO1 channels are activated solely through IP_3R-dependent Ca^{2+} signaling (see below). The ANO1-IP_3R1 and TRPV1-IP_3R1 clusters were fewer in quantity overall (which was also consistent with the PLA data), suggesting that physical interaction with IP_3Rs involves both ANO1 and TRPV1 association; this is also supported by the statistically significant reduction in functional TRPV1-ANO1 coupling after ER Ca^{2+} store depletion. Similar signaling nanodomains may exist in other neuron types, and close association of B_2Rs at the PM and IP_3Rs at the ER membrane has been reported in sympathetic neurons (*64*, *65*). Here, we propose that a close-proximity arrangement of ANO1, TRPV1, and IP_3R in DRG neurons ensures that Ca^{2+} influx through TRPV1 provides sufficiently high local [Ca^{2+}] to activate PLCδ, thus ultimately stimulating juxtaposed IP_3Rs that are in direct contact with ANO1 (Fig. 8D) [(*19*, *49*); present study].

As mentioned, our data do not exclude direct coupling between TRPV1 and ANO1, whereby Ca^{2+} influx through the former directly gates the latter (Fig. 8D, middle). Some neurons in our assays still produced Ca^{2+}-activated Cl^- currents in response to capsaicin under conditions of ER Ca^{2+} depletion (Fig. 4, B and C, and fig. S2C). STORM data suggest that although most of the multichannel complexes are composed of all three proteins, there is still a subpopulation of complexes consisting of only ANO1 and TRPV1, which may mediate such responses independently of IP_3R activation or serve as "specialized" heat sensors, only responding to noxious heat. Nevertheless, in the majority of neurons, ER Ca^{2+} release provides at least 50% or more of the Ca^{2+} ions necessary for the full activation of ANO1 by capsaicin-induced TRPV1 activation. This finding and the predominance of ANO1-TRPV1-IP_3R1 complexes over TRPV1-ANO1 complexes (Fig. 8C) collectively suggest that IP_3R-mediated Ca^{2+} release is indeed a critical factor for TRPV1-ANO1 coupling in sensory neurons.

One cannot exclude the existence of more intricate mechanisms, such as what was previously suggested for the CRAC-ANO1 interplay (*58*). For instance, Ca^{2+} entering the cytosol through TRPV1 could be taken into the ER by the SERCA pump and then re-released onto the ANO1 channels. The necessity of CRAC to refill the ER stores suggests another intriguing question: whether the association of the multichannel junctional complex reported here is static or being induced (or modified) in response to G_qPCR activation. Orai1 and STIM1 proteins form de novo junctional complexes to assemble into CRAC channels in response to the G_qPCR-induced store depletion (*66*). Could individual components of ANO1-containing signaling complexes assemble in a similar way upon stimulation? Further research is needed to investigate the dynamics of ANO1-TRPV1-IP_3R1 complex and its possible relationships with CRAC induction mechanisms.

The coupling between the TRPV1 and ANO1 channels in sensory neurons may hold a key to understanding thermal hypersensitivity (hyperalgesia) often produced by local inflammation. A functional and/or physical interaction between TRPV1 and ANO1 channels in nociceptors might enable ANO1 to act as an "amplifier" of TRPV1-mediated excitation, similar to the role of ANO2-mediated Ca^{2+}-activated Cl^- currents in olfactory neurons (*67*, *68*). The contribution of ANO1 activation, which in sensory neurons is excitatory, could then increase the dynamic range of the electrochemical response to noxious heat or inflammation by nociceptors, and this coupling may become more important in chronic pain, because the up-regulation of both TRPV1 and ANO1 expression in several pain models have been reported (*26*, *69*). It is also important to mention that ANO1 is a downstream component of various inflammatory mediator signaling cascades, which makes it an important player in inflammatory or chronic pain syndromes. The assembly of ANO1 into "junctional" nanodomains in pain-sensing neurons could also explain how Ca^{2+} signals induced by the relevant stimuli, such as inflammatory mediators or heat, can cause ANO1-mediated excitation, whereas "irrelevant" Ca^{2+} signals (such as those generated by VGCC during action potential firing) are precluded from having such an effect. Thus, the discovered mechanism exemplifies intricate wiring of intracellular Ca^{2+} signals in neurons providing for a high level of specificity and fidelity of intracellular signaling.

MATERIALS AND METHODS

Cell culture and transfection

DRGs were extracted from 7-day-old Westar rats, and neurons were dissociated as previously described (*8*, *19*). Cultures were maintained on 10-mm glass coverslips precoated with poly-D-lysine and laminin, and cells were left to grow for 48 hours in Dulbecco's modified Eagle's medium supplemented with GlutaMAX I (Invitrogen), 10% fetal bovine serum, penicillin (50 U/ml), and streptomycin (50 μg/ml) in a humidified incubator (5% CO_2, 37°C). For transfection with the EYFP-QL or CEPIA constructs, the Lonza Nucleofector I was used, and transfection was done before plating out the cells as described (*70*).

Live imaging

DRG cultures were loaded with 2 μM fura-2 AM (Life Technologies) in the presence of 0.01% pluronic F-127 (Sigma-Aldrich) at 37°C for

Downloaded from http://stke.sciencemag.org/ on May 3, 2020

45 min. Imaging was done using a Nikon TE-2000 microscope (inverted) with a 40× objective, and the imaging setup consisted of a Polychrome V monochromator, IMAGO charge-coupled device camera, and TILLVision 4.5.56 (Till Photonics) or Live Acquisition 2.2.0 (FEI) software packages. For standard fura-2 imaging (no EYFP-QL transfection), excitation at 340 and 380 nm was performed. For fluo-4 imaging, untransfected cells were loaded with fluo-4 AM using the same method as for fura-2 AM loading. An imaging system, comprising a Nikon TE-2000 E microscope with a DQC-FS camera and a LiveScan Swept Field confocal system, was used for fluo-4 imaging. Analysis was done using Nikon Elements software.

To simultaneously image Ca^{2+} and I^-, DRG neurons (~20 μm in diameter) successfully transfected with EYFP-QL and loaded with fura-2 were selected for imaging; glial cells (identified by bipolar processes) were excluded from the analyses. The simultaneous Ca^{2+}/I^- imaging was performed using the UV-2A filter cube (Nikon), and excitation was performed at 340/380 (fura-2) and 488 nm (EYFP-QL) wavelengths. Exposure time (typically within 50 to 200 ms for fura-2 and 400 to 500 ms for EYFP-QL) was set for each wavelength on a cell-to-cell basis, depending on the basal fluorescence intensity. For quadruple-wavelength imaging, DRG neurons (transfected with EYFP-QL) loaded with fura-2 were imaged using 340, 380, 488, and 560 nm wavelength light using a custom-made dichroic/filter combination DC/59022bs-XR-360-UF1 and DC/59022m (Chroma).

Standard extracellular bath solution consisted of the following: NaCl (160 mM), KCl (2.5 mM), $MgCl_2$ (1 mM), $CaCl_2$ (2 mM), Hepes (10 mM), and glucose (10 mM); pH adjusted to 7.4 with NaOH (all from Sigma-Aldrich). I^--containing solutions were produced by equimolar substitution of the NaCl with NaI (30, 10, or 5 mM). Compounds were added to the NaI-containing solution while imaging: GABA, 100 μM (Tocris); capsaicin, 1 μM (Sigma-Aldrich); BK, 250 nM (Merck); RR, 10 μM (Sigma-Aldrich). K2 was a gift from A. Priel (The Institute for Drug Research, School of Pharmacy, Faculty of Medicine, The Hebrew University of Jerusalem). The depolarizing 50 mM K^+ solution was produced by equimolar substitution of NaCl with KCl. Ca^{2+}-free solutions were produced with increased NaCl (165 mM) to compensate for Cl^- lost with the removal of $CaCl_2$; 1 mM EGTA was also added. Preincubation with TG (1 μM; LKT Laboratories) or CPA (1 μM; Tocris) was done during the fura-2 loading process where required, and the compound was also kept in solutions throughout imaging. Gravity bath perfusion was used for all experiments apart from those involving K2, for which an Automate Scientific SmartSquirt Microperfusion system was used. A fine 100-μm tip was used with this system, and pressure was maintained at 3 psi for all experiments using this perfusion method. The tip was positioned over DRG neurons selected for testing under ×10 or ×40 magnification before being activated.

Imaging data analysis

Analysis of primary data and statistics were performed in Microsoft Excel, Origin Pro, and GraphPad Prism 8. Fura-2 ratios were normalized to R value at $t = 0$ (R_0) and expressed as a difference from R/R_0 ($\Delta R/R_0$). EYFP-QL fluorescence intensity was normalized to fluorescence at $t = 0$ (F_0) and expressed as a difference from F_0 ($\Delta F/F_0$), for each cell. Data from all cells were temporarily aligned to the point of R/R_0 increase by three times the SD of the baseline. Agonist-dependent EYFP-QL fluorescence quenching or red-CEPIA fluorescence intensity change was quantified from this point until the end of agonist application. Where possible, linear agonist-independent rundown of fluorescence signals was corrected before the final analysis.

Electrophysiology

Whole-cell voltage-clamp recordings were performed as previously described (*8*). Patch electrodes were pulled from borosilicate glass and fire polished to a final resistance of 2 to 4 megaohms. An EPC-10 patch-clamp amplifier in combination with Patchmaster version 2x35 software (HEKA) was used. Standard extracellular bath solution consisted of the following: NaCl (160 mM), KCl (2.5 mM), $MgCl_2$ (1 mM), $CaCl_2$ (2 mM), Hepes (10 mM), and glucose (10 mM); pH adjusted to 7.4 with NaOH (all from Sigma-Aldrich). The internal pipette solution consisted of the following: CsCl (150 mM), $MgCl_2$ (5 mM), K_2ATP (1 mM), NaGTP (0.1 mM), EGTA (1 mM), and Hepes (10 mM); pH adjusted to 7.4 with CsOH (all from Sigma-Aldrich). After obtaining a gigaseal, whole-cell configuration was attained, and gap-free recordings were performed at a holding voltage of −60 mV. Capsaicin (1 μM) was applied to DRG neurons with or without 30-min preincubation with Ani9 (500 nM; Tocris) or TG (1 μM). Fitmaster v2x73.5 (HEKA) has been used for data analysis.

PLCδ-PH-GFP translocation

Cultured DRG neurons were transfected with the PLCδ-PH-GFP construct using the same method as for EYFP-QL and CEPIA transfection (see above). The Nikon confocal imaging and analysis system used for fluo-4 AM live Ca^{2+} imaging were also used for PLCδ-PH-GFP translocation assays. GFP fluorescence intensity in the cytosolic regions of the cell was used as a measure of the probe translocation.

Proximity ligation assay

PLA was performed using PLA kits (Sigma-Aldrich) as previously described (*19*). Antibodies used were ANO1 (1:200; Santa Cruz or 1:500; Abcam), TRPV1 (1:500; Neuromics), IP_3R1 (1:500; Calbiochem), and CD71 (1:500; Santa Cruz). For anti–guinea pig antibodies (such as TRPV1), PLA "minus" probes were manually conjugated onto an anti–guinea pig immunoglobulin G antibody using a PLA conjugation kit. DRG cultures were prepared and plated on microscope slides (coated with poly-D-lysine and laminin) and permeabilized using acetone:methanol (1:1) on ice for 20 min and washed with phosphate-buffered saline three times. Hydrophobic barriers were made on the slides using an ImmEdge hydrophobic barrier pen (Vector Laboratories) to delimit reactions to ~1 cm^2, and blocking was done using the PLA blocking reagent for 30 min in a humidified incubator (37°C). Primary antibodies were then applied and left at 4°C overnight. The following day, PLA probes were applied to the samples, signals were amplified and detected according to the manufacturer's instructions, and slides were sealed with 4′,6-diamidino-2-phenylindole–containing mounting medium (Sigma-Aldrich). Samples were imaged using the Zeiss LSM700 confocal microscope. Green fluorescent puncta (0.5 to 1 μm) were counted per cell using Zen imaging software (Zeiss).

Statistical analysis

Data are presented as means ± SEM unless stated. Data were tested for normality, and either parametric [Student's t test and analysis of variance (ANOVA)] or nonparametric (Wilcoxon signed-rank test, Mann-Whitney test, and Kruskal-Wallis ANOVA) tests were carried out. Difference between means was considered statistically significant at $P < 0.05$. Approach to analysis of STORM data is described below.

Downloaded from http://stke.sciencemag.org/ on May 3, 2020

Stochastic optical reconstruction microscopy

All images were acquired on a Nikon N-STORM superresolution system (Nikon Instruments Inc.), consisting of a Nikon Eclipse Ti inverted microscope and an astigmatic 3D lens placed in front of the EMCCD camera to allow the Z coordinates to be most accurately determined. The laser setup of our STORM system allows for the multiple, largely nonoverlapping activator dyes, Alexa Fluor 405 carboxylic acid (Invitrogen, #A30000), Cy2 bisreactive dye pack (GE Healthcare, #PA22000), and Cy3 mono-reactive dye pack (GE Healthcare, #PA23001), to be conjugated to affinity-purified secondary antibodies from Jackson ImmunoResearch, along with the reporter dye, Alexa Fluor 647 carboxylic acid (Invitrogen, #A20006) to acquire images from three different protein labels in the same experiment. Using the same primary antibodies used in the PLA experiments, we determined the extent of colocalization of TRPV1, ANO1, and IP_3R1, as individual multiprotein complexes with either two or three photo-switchable dye activators, Alexa Fluor 405, Cy2, and Cy3, coupled to three distinct secondary antibodies (raised in different species) labeling the proteins in DRGs. The activator and reporter fluorophores were conjugated in-house to an appropriate unlabeled secondary antibody (*71*). STORM imaging was performed in a freshly prepared imaging buffer that contained the following: 50 mM tris (pH 8.0), 10 mM NaCl, and 10% (w/v) glucose, with an oxygen-scavenging GLOX solution [glucose oxidase (0.5 mg/ml; Sigma-Aldrich), catalase (40 μg/ml; Sigma-Aldrich), and 10 mM β-mercaptoethylamine (MEA, Sigma-Aldrich). MEA was prepared fresh as a 1 M stock solution in water, stored at 4°C, and used within 1 month of preparation. Acquisitions were made from between two and four different experiments for labeling and imaging. Images were rendered as a 2D Gaussian fit of each localization. The diameter of each point is representative of the localization precision (larger diameter, less precise), as is intensity (more intense, more precise). Signal-noise thresholds were handled as peak height above the local background in the N-STORM software (Elements). A detected peak was set as the central pixel in a 5 × 5 pixel area, and the average intensity of the four corner pixels was subtracted from the intensity of the central pixel. Using a 100× objective and 16 μm × 16 μm pixel area of the iXon3 camera, this corresponds to a 0.8 μm × 0.8 μm physical neighborhood.

Adjustment of STORM localizations for differential rates of dye bleaching

The STORM acquisitions were carried out for a minimum of 6000 activator-reporter cycles and until at least one of three activator laser wavelengths no longer registered localizations. We observed that the Alexa Fluor 405–Alexa Fluor 647 dye pair persisted stably for more cycles than the Cy2–Alexa Fluor 647 or Cy3–Alexa Fluor 647 dye pairs, independent of the secondary antibody that was conjugated (fig. S8). Therefore, we concluded that the Cy2 and Cy3 dyes bleach out more rapidly than Alexa Fluor 405 after many repeated activation cycles. Such differential rates of photobleaching would cause us to overestimate the number of complexes containing a protein labeled by Alexa Fluor 405 and possibly underestimate those without. Hence, we corrected for this artifact to the best of our ability. To more adequately compare the STORM localizations in the triple-labeled conditions, we first determined a linear approximation of the differential exponential decay of localizations for each corresponding activator dye. The cumulative probability distributions demonstrated that Alexa Fluor 405 had a statistically significantly greater number of localizations than equally labeled Cy2 or Cy3 at about 3000 laser activation cycles (36,000 total frames) and beyond (fig. S8). The factor of decay was used to time-dependently correct for this by probabilistically excluding Alexa Fluor 405–specific localizations from the cluster detection analysis to compensate for this, preventing oversampling above that of Cy2 or Cy3 molecules. After this adjustment, the numbers of clusters of each combination of multichannel complexes did not statistically significantly change due to the details of our sampling paradigm, except for those of Alexa Fluor 405–only centroid clusters. We estimate that the applied compensation paradigm corrected for the above mentioned artifact by >90%.

Cluster size and localization proximity analysis

Unfiltered STORM localization data were exported as molecular list text files from Nikon Elements and were analyzed with in-house software incorporating a DBSCAN (*72*). A dense region or cluster was defined as localizations within a directly reachable radius proximity (epsilon) from a criterion minimum number of other core localizations (MinPts). Density-reachable points were localizations that were within the epsilon radius of a single core point and thus considered part of the cluster. Localizations considered to be noise were points that were not within the epsilon distance of any core points of a cluster. We derived the appropriate epsilon parameter using the nearest-neighbor plot from single-dye labeled controls; cluster detection was determined for epsilon between 20 and 80 nm, which were the nearest-neighbor localization distances representing 95% of A.U.C. DBSCAN parameters were verified by measuring goodness of fit to Gaussian distribution with cluster population data from single-dye labeled controls and set for distance of directly reachable points at 50 nm (epsilon) and seven minimum points (MinPts). These parameters were found to be the most stringent possible that also reliably fit the control data. For cluster detection, each localization was assessed on the basis of its corrected X and corrected Y 2D spatial coordinates, and the associated activator dye was tracked throughout analysis. Detected clusters were tabulated by the composition of resident activator dyes contributing to the total neighborhood of localizations for that cluster. Clusters were categorized on the basis of activator dye composition as Alexa Fluor 405 only, Cy2 only, Cy3 only, Alexa Fluor 405 + Cy2, Alexa Fluor 405 + Cy3, or Alexa Fluor 405 + Cy2 + Cy3, according to the dye conjugated to each antibody label. Cluster radius size (nm) data were placed in probability distribution histograms with bin size of 5 nm. On the basis of the observation that a majority of cluster distributions displayed positive skew, distributions were fit by the generalized extreme value distribution function: $f(x) = e^{-(x-1 + e\text{^}-x)}$. Cluster size values were reported as means ± SEM. The β continuous scale parameter of each cluster distribution was derived from the mean value of the extreme distribution (mean = μ + γβ, γ: 0.5772, Euler-Mascheroni constant) and was determined as a metric for "tailedness" of cluster size distribution. In addition, the percentage of clusters belonging to a labeling category out of total clusters was compared. Cumulative distribution functions of cluster categories were compared with the Kolmogorov-Smirnov test. Population statistics for each cluster category were derived from 6 to 12 cells per staining and imaging condition.

SUPPLEMENTARY MATERIALS

stke.sciencemag.org/cgi/content/full/13/629/eaaw7963/DC1

Fig. S1. Depolarization-induced I^- influx is a Ca^{2+}-independent phenomenon.

Fig. S2. ER Ca^{2+} store depletion severely reduces Ca^{2+} transients and CaCC activation in response to capsaicin.

Downloaded from http://stke.sciencemag.org/ on May 3, 2020

Fig. S3. Capsaicin applied in extracellular Ca^{2+}-free conditions and acute TG-induced ER Ca^{2+} leak can induce a degree of CaCC activation.
Fig. S4. The cell-impermeable TRPV1 agonist K2 evokes cytosolic Ca^{2+} transients in the absence of extracellular Ca^{2+}.
Fig. S5. Capsaicin induces PLC activation in DRG neurons.
Fig. S6. Controls for PLA.
Fig. S7. CD71 and IP_3R1 are not found in close proximity as confirmed by PLA and STORM analysis.
Fig. S8. Decay rates of STORM fluorescent dye labels after repeated laser activation cycles.
Table S1. Mean percentages of STORM cluster distributions detected by DBSCAN.
Table S2. Mean cluster radius sizes of STORM-derived clusters detected by DBSCAN.
Table S3. Mean number of localizations per cluster from STORM-derived clusters detected by DBSCAN.

View/request a protocol for this paper from *Bio-protocol*.

REFERENCES AND NOTES

1. X. Jin, S. Shah, X. Du, H. Zhang, N. Gamper, Activation of Ca^{2+}-activated Cl^- channel ANO1 by localized Ca^{2+} signals. *J. Physiol.* **594**, 19–30 (2016).
2. C. Hartzell, I. Putzier, J. Arreola, Calcium-activated chloride channels. *Annu. Rev. Physiol.* **67**, 719–758 (2005).
3. N. Pedemonte, L. J. V. Galietta, Structure and function of TMEM16 proteins (anoctamins). *Physiol. Rev.* **94**, 419–459 (2014).
4. F. Huang, X. Wong, L. Y. Jan, International Union of Basic and Clinical Pharmacology. LXXXV: Calcium-activated chloride channels. *Pharmacol. Rev.* **64**, 1–15 (2012).
5. A. Caputo, E. Caci, L. Ferrera, N. Pedemonte, C. Barsanti, E. Sondo, U. Pfeffer, R. Ravazzolo, O. Zegarra-Moran, L. J. V. Galietta, TMEM16A, a membrane protein associated with calcium-dependent chloride channel activity. *Science* **322**, 590–594 (2008).
6. B. C. Schroeder, T. Cheng, Y. N. Jan, L. Y. Jan, Expression cloning of TMEM16A as a calcium-activated chloride channel subunit. *Cell* **134**, 1019–1029 (2008).
7. Y. D. Yang, H. Cho, J. Y. Koo, M. H. Tak, Y. Cho, W.-S. Shim, S. P. Park, J. Lee, B. Lee, B.-M. Kim, R. Raouf, Y. K. Shin, U. Oh, TMEM16A confers receptor-activated calcium-dependent chloride conductance. *Nature* **455**, 1210–1215 (2008).
8. B. Liu, J. E. Linley, X. Du, X. Zhang, L. Ooi, H. Zhang, N. Gamper, The acute nociceptive signals induced by bradykinin in rat sensory neurons are mediated by inhibition of M-type K^+ channels and activation of Ca^{2+}-activated Cl^- channels. *J. Clin. Invest.* **120**, 1240–1252 (2010).
9. H. Cho, Y. D. Yang, J. Lee, B. Lee, T. Kim, Y. Jang, S. K. Back, H. S. Na, B. D. Harfe, F. Wang, R. Raouf, J. N. Wood, U. Oh, The calcium-activated chloride channel anoctamin 1 acts as a heat sensor in nociceptive neurons. *Nat. Neurosci.* **15**, 1015–1021 (2012).
10. Y. Takayama, D. Uta, H. Furue, M. Tominaga, Pain-enhancing mechanism through interaction between TRPV1 and anoctamin 1 in sensory neurons. *Proc. Natl. Acad. Sci. U.S.A.* **112**, 5213–5218 (2015).
11. K. Funk, A. Woitecki, C. Franjic-Wurtz, T. Gensch, F. Möhrlen, S. Frings, Modulation of chloride homeostasis by inflammatory mediators in dorsal root ganglion neurons. *Mol. Pain* **4**, 32 (2008).
12. S. Pieraut, V. Laurent-Matha, C. Sar, T. Hubert, I. Méchaly, C. Hilaire, M. Mersel, E. Delpire, J. Valmier, F. Scamps, NKCC1 phosphorylation stimulates neurite growth of injured adult sensory neurons. *J. Neurosci.* **27**, 6751–6759 (2007).
13. Q. Xiao, K. Yu, P. Perez-Cornejo, Y. Cui, J. Arreola, H. C. Hartzell, Voltage- and calcium-dependent gating of TMEM16A/Ano1 chloride channels are physically coupled by the first intracellular loop. *Proc. Natl. Acad. Sci. U.S.A.* **108**, 8891–8896 (2011).
14. C. Paulino, V. Kalienkova, A. K. M. Lam, Y. Neldner, R. Dutzler, Activation mechanism of the calcium-activated chloride channel TMEM16A revealed by cryo-EM. *Nature* **552**, 421–425 (2017).
15. J. A. Contreras-Vite, S. Cruz-Rangel, J. J. De Jesús-Pérez, I. A. A. Figueroa, A. A. Rodríguez-Menchaca, P. Pérez-Cornejo, H. C. Hartzell, J. Arreola, Revealing the activation pathway for TMEM16A chloride channels from macroscopic currents and kinetic models. *Pflugers Arch.* **468**, 1241–1257 (2016).
16. X. Du, H. Hao, S. Gigout, D. Huang, Y. Yang, L. Li, C. Wang, D. Sundt, D. B. Jaffe, H. Zhang, N. Gamper, Control of somatic membrane potential in nociceptive neurons and its implications for peripheral nociceptive transmission. *Pain* **155**, 2306–2322 (2014).
17. D. Sapunar, M. Ljubkovic, P. Lirk, J. B. McCallum, Q. H. Hogan, Distinct membrane effects of spinal nerve ligation on injured and adjacent dorsal root ganglion neurons in rats. *Anesthesiology* **103**, 360–376 (2005).
18. R. Amir, C.-N. Liu, J. D. Kocsis, M. Devor, Oscillatory mechanism in primary sensory neurones. *Brain* **125**, 421–435 (2002).
19. X. Jin, S. Shah, Y. Liu, H. Zhang, M. Lees, Z. Fu, J. D. Lippiat, D. J. Beech, A. Sivaprasadarao, S. A. Baldwin, H. Zhang, N. Gamper, Activation of the Cl^- channel ANO1 by localized calcium signals in nociceptive sensory neurons requires coupling with the IP_3 receptor. *Sci. Signal.* **6**, ra73 (2013).
20. S. M. Ward, J. L. Kenyon, The spatial relationship between Ca^{2+} channels and Ca^{2+}-activated channels and the function of Ca^{2+}-buffering in avian sensory neurons. *Cell Calcium* **28**, 233–246 (2000).
21. R. Bao, L. M. Lifshitz, R. A. Tuft, K. Bellvé, K. E. Fogarty, R. ZhuGe, A close association of RyRs with highly dense clusters of Ca^{2+}-activated Cl^- channels underlies the activation of STICs by Ca^{2+} sparks in mouse airway smooth muscle. *J. Gen. Physiol.* **132**, 145–160 (2008).
22. P. J. Bauer, The local Ca concentration profile in the vicinity of a Ca channel. *Cell Biochem. Biophys.* **35**, 49–61 (2001).
23. R. Rizzuto, T. Pozzan, Microdomains of intracellular Ca^{2+}: Molecular determinants and functional consequences. *Physiol. Rev.* **86**, 369–408 (2006).
24. J. E. Linley, K. Rose, L. Ooi, N. Gamper, Understanding inflammatory pain: Ion channels contributing to acute and chronic nociception. *Pflugers Arch.* **459**, 657–669 (2010).
25. G. Pethő, P. W. Reeh, Sensory and signaling mechanisms of bradykinin, eicosanoids, platelet-activating factor, and nitric oxide in peripheral nociceptors. *Physiol. Rev.* **92**, 1699–1775 (2012).
26. B. Lee, H. Cho, J. Jung, Y. D. Yang, D.-J. Yang, U. Oh, Anoctamin 1 contributes to inflammatory and nerve-injury induced hypersensitivity. *Mol. Pain* **10**, 5 (2014).
27. F. Ru, H. Sun, D. Jurcakova, R. A. Herbstsomer, J. Meixong, X. Dong, B. J. Undem, Mechanisms of pruritogen-induced activation of itch nerves in isolated mouse skin. *J. Physiol.* **595**, 3651–3666 (2017).
28. K. Kunzelmann, I. Cabrita, P. Wanitchakool, J. Ousingsawat, L. Sirianant, R. Benedetto, R. Schreiber, Modulating Ca^{2+} signals: A common theme for TMEM16, Ist2, and TMC. *Pflugers Arch.* **468**, 475–490 (2016).
29. Y. Dai, T. Moriyama, T. Higashi, K. Togashi, K. Kobayashi, H. Yamanaka, M. Tominaga, K. Noguchi, Proteinase-activated receptor 2-mediated potentiation of transient receptor potential vanilloid subfamily 1 activity reveals a mechanism for proteinase-induced inflammatory pain. *J. Neurosci.* **24**, 4293–4299 (2004).
30. D. S. K. Samways, B. S. Khakh, T. M. Egan, Tunable calcium current through TRPV1 receptor channels. *J. Biol. Chem.* **283**, 31274–31278 (2008).
31. V. Lukacs, Y. Yudin, G. R. Hammond, E. Sharma, K. Fukami, T. Rohacs, Distinctive changes in plasma membrane phosphoinositides underlie differential regulation of TRPV1 in nociceptive neurons. *J. Neurosci.* **33**, 11451–11463 (2013).
32. L. J. V. Galietta, P. M. Haggie, A. S. Verkman, Green fluorescent protein-based halide indicators with improved chloride and iodide affinities. *FEBS Lett.* **499**, 220–224 (2001).
33. T. Johansson, T. Norris, H. Peilot-Sjögren, Yellow fluorescent protein-based assay to measure $GABA_A$ channel activation and allosteric modulation in CHO-K1 cells. *PLOS ONE* **8**, e59429 (2013).
34. W. Namkung, Z. Yao, W. E. Finkbeiner, A. S. Verkman, Small-molecule activators of TMEM16A, a calcium-activated chloride channel, stimulate epithelial chloride secretion and intestinal contraction. *FASEB J.* **25**, 4048–4062 (2011).
35. X. Du, H. Hao, Y. Yang, S. Huang, C. Wang, S. Gigout, R. Ramli, X. Li, E. Jaworska, I. Edwards, J. Deuchars, Y. Yanagawa, J. Qi, B. Guan, D. B. Jaffe, H. Zhang, N. Gamper, Local GABAergic signaling within sensory ganglia controls peripheral nociceptive transmission. *J. Clin. Invest.* **127**, 1741–1756 (2017).
36. B. Robertson, Characteristics of GABA-activated chloride channels in mammalian dorsal root ganglion neurones. *J. Physiol.* **411**, 285–300 (1989).
37. J. P. Gallagher, H. Higashi, S. Nishi, Characterization and ionic basis of GABA-induced depolarizations recorded in vitro from cat primary afferent neurones. *J. Physiol.* **275**, 263–282 (1978).
38. Y. Seo, H. K. Lee, J. Park, D.-k. Jeon, S. Jo, M. Jo, W. Namkung, Ani9, a novel potent small-molecule ANO1 inhibitor with negligible effect on ANO2. *PLOS ONE* **11**, e0155771 (2016).
39. L. S. Premkumar, G. P. Ahern, Induction of vanilloid receptor channel activity by protein kinase C. *Nature* **408**, 985–990 (2000).
40. J. Suzuki, K. Kanemaru, K. Ishii, M. Ohkura, Y. Okubo, M. Iino, Imaging intraorganellar Ca^{2+} at subcellular resolution using CEPIA. *Nat. Commun.* **5**, 4153 (2014).
41. V. Lukacs, B. Thyagarajan, P. Varnai, A. Balla, T. Balla, T. Rohacs, Dual regulation of TRPV1 by phosphoinositides. *J. Neurosci.* **27**, 7070–7080 (2007).
42. K. C. Thomas, A. S. Sabnis, M. E. Johansen, D. L. Lanza, P. J. Moos, G. S. Yost, C. A. Reilly, Transient receptor potential vanilloid 1 agonists cause endoplasmic reticulum stress and cell death in human lung cells. *J. Pharmacol. Exp. Ther.* **321**, 830–838 (2007).
43. C. J. Bohlen, A. Priel, S. Zhou, D. King, J. Siemens, D. Julius, A bivalent tarantula toxin activates the capsaicin receptor, TRPV1, by targeting the outer pore domain. *Cell* **141**, 834–845 (2010).
44. E. Cao, M. Liao, Y. Cheng, D. Julius, TRPV1 structures in distinct conformations reveal activation mechanisms. *Nature* **504**, 113–118 (2013).
45. C. Bae, C. Anselmi, J. Kalia, A. Jara-Oseguera, C. D. Schwieters, D. Krepkiy, C. Won Lee, E.-H. Kim, J. I. Kim, J. D. Faraldo-Gómez, K. J. Swartz, Structural insights into the mechanism of activation of the TRPV1 channel by a membrane-bound tarantula toxin. *eLife* **5**, e11273 (2016).
46. M. Geron, R. Kumar, W. Zhou, J. D. Faraldo-Gómez, V. Vásquez, A. Priel, TRPV1 pore turret dictates distinct DkTx and capsaicin gating. *Proc. Natl. Acad. Sci. U.S.A.* **115**, E11837–E11846 (2018).

Downloaded from http://stke.sciencemag.org/ on May 3, 2020

47. N. Gamper, T. Rohacs, Phosphoinositide sensitivity of ion channels, a functional perspective. *Subcell. Biochem.* **59**, 289–333 (2012).
48. E. J. Dickson, B. Hille, Understanding phosphoinositides: Rare, dynamic, and essential membrane phospholipids. *Biochem. J.* **476**, 1–23 (2019).
49. I. Cabrita, R. Benedetto, A. Fonseca, P. Wanitchakool, L. Sirianant, B. V. Skryabin, L. K. Schenk, H. Pavenstädt, R. Schreiber, K. Kunzelmann, Differential effects of anoctamins on intracellular calcium signals. *FASEB J.* **31**, 2123–2134 (2017).
50. I. Weibrecht, K.-J. Leuchowius, C.-M. Clausson, T. Conze, M. Jarvius, W. M. Howell, M. Kamali-Moghaddam, O. Söderberg, Proximity ligation assays: A recent addition to the proteomics toolbox. *Expert Rev. Proteomics* **7**, 401–409 (2010).
51. O. Söderberg, M. Gullberg, M. Jarvius, K. Ridderstråle, K. J. Leuchowius, J. Jarvius, K. Wester, P. Hydbring, F. Bahram, L.-G. Larsson, U. Landegren, Direct observation of individual endogenous protein complexes in situ by proximity ligation. *Nat. Methods* **3**, 995–1000 (2006).
52. J. Zhang, C. M. Carver, F. S. Choveau, M. S. Shapiro, Clustering and functional coupling of diverse ion channels and signaling proteins revealed by super-resolution STORM microscopy in neurons. *Neuron* **92**, 461–478 (2016).
53. M. Amsalem, C. Poilbout, G. Ferracci, P. Delmas, F. Padilla, Membrane cholesterol depletion as a trigger of Nav1.9 channel-mediated inflammatory pain. *EMBO J.* **37**, e97349 (2018).
54. A. Dani, B. Huang, J. Bergan, C. Dulac, X. Zhuang, Superresolution imaging of chemical synapses in the brain. *Neuron* **68**, 843–856 (2010).
55. M. J. Rust, M. Bates, X. Zhuang, Sub-diffraction-limit imaging by stochastic optical reconstruction microscopy (STORM). *Nat. Methods* **3**, 793–796 (2006).
56. D. Axelrod, Total internal reflection fluorescence microscopy in cell biology. *Methods Enzymol.* **361**, 1–33 (2003).
57. M. Bal, O. Zaika, P. Martin, M. S. Shapiro, Calmodulin binding to M-type K^+ channels assayed by TIRF/FRET in living cells. *J. Physiol.* **586**, 2307–2320 (2008).
58. R. Courjaret, K. Machaca, Mid-range Ca^{2+} signalling mediated by functional coupling between store-operated Ca^{2+} entry and IP_3-dependent Ca^{2+} release. *Nat. Commun.* **5**, 3916 (2014).
59. T. Rohacs, Phosphoinositide signaling in somatosensory neurons. *Adv. Biol. Regul.* **61**, 2–16 (2016).
60. S. Gallego-Sandin, A. Rodríguez-García, M. T. Alonso, J. García-Sancho, The endoplasmic reticulum of dorsal root ganglion neurons contains functional TRPV1 channels. *J. Biol. Chem.* **284**, 32591–32601 (2009).
61. N. A. Jeske, Somatosensory scaffolding structures. *Front. Mol. Neurosci.* **5**, 2 (2012).
62. N. A. Jeske, K. A. Berg, J. C. Cousins, E. S. Ferro, W. P. Clarke, M. J. Glucksman, J. L. Roberts, Modulation of bradykinin signaling by EP24.15 and EP24.16 in cultured trigeminal ganglia. *J. Neurochem.* **97**, 13–21 (2006).
63. E. Szőke, R. Börzsei, D. M. Tóth, O. Lengl, Z. Helyes, Z. Sándor, J. Szolcsányi, Effect of lipid raft disruption on TRPV1 receptor activation of trigeminal sensory neurons and transfected cell line. *Eur. J. Pharmacol.* **628**, 67–74 (2010).
64. P. Delmas, N. Wanaverbecq, F. C. Abogadie, M. Mistry, D. A. Brown, Signaling microdomains define the specificity of receptor-mediated $InsP_3$ pathways in neurons. *Neuron* **34**, 209–220 (2002).
65. N. Gamper, V. Reznikov, Y. Yamada, J. Yang, M. S. Shapiro, Phosphatidylinositol 4,5-bisphosphate signals underlie receptor-specific $G_{q/11}$-mediated modulation of N-type Ca^{2+} channels. *J. Neurosci.* **24**, 10980–10992 (2004).
66. M. D. Cahalan, STIMulating store-operated Ca^{2+} entry. *Nat. Cell Biol.* **11**, 669–677 (2009).
67. S. Pifferi, V. Cenedese, A. Menini, Anoctamin 2/TMEM16B: A calcium-activated chloride channel in olfactory transduction. *Exp. Physiol.* **97**, 193–199 (2012).
68. A. B. Stephan, E. Y. Shum, S. Hirsh, K. D. Cygnar, J. Reisert, H. Zhao, ANO2 is the cilial calcium-activated chloride channel that may mediate olfactory amplification. *Proc. Natl. Acad. Sci. U.S.A.* **106**, 11776–11781 (2009).
69. Y. Kanai, E. Nakazato, A. Fujiuchi, T. Hara, A. Imai, Involvement of an increased spinal TRPV1 sensitization through its up-regulation in mechanical allodynia of CCI rats. *Neuropharmacology* **49**, 977–984 (2005).
70. H. M. Kirton, L. Pettinger, N. Gamper, Transient overexpression of genes in neurons using nucleofection. *Methods Mol. Biol.* **998**, 55–64 (2013).
71. G. T. Dempsey, J. C. Vaughan, K. H. Chen, M. Bates, X. Zhuang, Evaluation of fluorophores for optimal performance in localization-based super-resolution imaging. *Nat. Methods* **8**, 1027–1036 (2011).
72. M. Ester, H.-P. Kriegel, J. Sander, X. Xu, A Density-Based Algorithm for Discovering Clusters in Large Spatial Datasets with Noise, in *Proceedings of the Second International Conference on Knowledge Discovery and Data Mining (KDD'96)* (AAAI Press, Portland, Oregon, 1996), pp. 1232–1239.

Acknowledgments: We thank G. Hoppen (University of Leeds) for assistance with PLA controls and A. Priel (The Institute for Drug Research, School of Pharmacy, Faculty of Medicine, The Hebrew University of Jerusalem) for the gift of the K2 toxin. **Funding:** This work was supported by the BBSRC grants BB/R02104X/1 and BB/R003068/1 to N.G., by the NIH grants R01 NS094461 and R01 NS043394 to M.S.S., by the Presidential Scholar award to M.S.S., and by a postdoctoral training fellowship to C.M.C. from Training Grant T32 HL007446 (James D. Stockand, PI). **Author contributions:** S.S., C.M.C., and N.G. designed experiments. S.S., C.M.C., P.M., S.M., V.L., and N.G. performed experiments and analyzed data. C.M.C. and M.S.S. developed the STORM approach and obtained and analyzed STORM data. All authors contributed to writing the manuscript. **Competing interests:** The authors declare that they have no competing interests. **Data and materials availability:** All data needed to evaluate the conclusions in the paper are present in the paper or the Supplementary Materials.

Submitted 25 January 2019
Resubmitted 2 December 2019
Accepted 2 April 2020
Published 28 April 2020
10.1126/scisignal.aaw7963

Citation: S. Shah, C. M. Carver, P. Mullen, S. Milne, V. Lukacs, M. S. Shapiro, N. Gamper, Local Ca^{2+} signals couple activation of TRPV1 and ANO1 sensory ion channels. *Sci. Signal.* **13**, eaaw7963 (2020).

Downloaded from http://stke.sciencemag.org/ on May 3, 2020

Science Signaling

Local Ca^{2+} signals couple activation of TRPV1 and ANO1 sensory ion channels

Shihab Shah, Chase M. Carver, Pierce Mullen, Stephen Milne, Viktor Lukacs, Mark S. Shapiro and Nikita Gamper

Sci. Signal. **13** (629), eaaw7963.
DOI: 10.1126/scisignal.aaw7963

Boosting the Ca^{2+} signal for nociception

The Ca^{2+}-activated Cl^- channel ANO1 promotes nociception, the perception of pain. The nonselective cation channel TRPV1 has been proposed to be the source of Ca^{2+} that activates ANO1, but the amount of Ca^{2+} that TRPV1 allows into pain-transmitting DRG neurons is thought to be insufficient to activate ANO1. Shah *et al.* found that TRPV1 triggered Ca^{2+} release from the ER through an IP_3 receptor isoform. Imaging techniques showed that ANO1, TRPV1, and the IP_3 receptor clustered in close proximity to each other in pain-transmitting DRG neurons. These results provide insight into the molecular mechanisms underlying nociception.

ARTICLE TOOLS http://stke.sciencemag.org/content/13/629/eaaw7963

SUPPLEMENTARY MATERIALS http://stke.sciencemag.org/content/suppl/2020/04/24/13.629.eaaw7963.DC1

RELATED CONTENT http://stke.sciencemag.org/content/sigtrans/6/290/ra73.full

REFERENCES This article cites 71 articles, 18 of which you can access for free
http://stke.sciencemag.org/content/13/629/eaaw7963#BIBL

PERMISSIONS http://www.sciencemag.org/help/reprints-and-permissions

Use of this article is subject to the Terms of Service

Science Signaling (ISSN 1937-9145) is published by the American Association for the Advancement of Science, 1200 New York Avenue NW, Washington, DC 20005. The title *Science Signaling* is a registered trademark of AAAS.

Copyright © 2020 The Authors, some rights reserved; exclusive licensee American Association for the Advancement of Science. No claim to original U.S. Government Works

Downloaded from http://stke.sciencemag.org/ on May 3, 2020